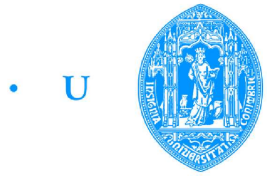

UNIVERSIDADE DE COIMBRA

Study of ATLAS sensitivity to asymmetries in single top events

Dissertação submetida para a obtenção do Grau de Mestre em Física Nuclear e de Partículas

Miguel Castro Nunes Fiolhais

Orientador: Professor Doutor António Joaquim Onofre de Abreu Ribeiro Gonçalves

Co-Orientador: Professor Doutor João Carlos Lopes Carvalho

Coimbra, 2008

Resumo

O estudo da sensibilidade da experiência ATLAS do LHC na medida de assimetrias angulares e de spin no canal-t da produção simples do quark top foi realizada utilizando simulação rápida do detector (ATLFAST) e todos os acontecimentos foram gerados recorrendo aos programas Pythia e TopReX. Por forma a obter uma selecção eficiente de acontecimentos, foi desenvolvida uma análise probabilística para uma luminosidade de 10 fb^{-1}. A partir dos resultados obtidos para as assimetrias, foram calculados os limites nos acoplamentos anómalos do vértice Wtb com um nível de confiança de $68,3\%$ utilizando o programa TopFit.

Abstract

The study of the LHC ATLAS experiment sensitivity to angular and spin asymmetries in the production of single top quarks (t-channel) events was done using the fast detector simulation (ATLFAST) and all the events were generated using Pythia and TopReX libraries. In order to get an efficient selection of events, a likelihood-based analysis was developed for a luminosity of 10 fb^{-1}. From the measurement of these asymmetries, the limits at 68.3% confidence level on the anomalous couplings of the Wtb vertex were set using the TopFit library.

Acknowledgements

First of all, I would like to thank to my supervisors, Professors António Onofre and João Carvalho, for their outstanding guidance and dedication. I also thank the support and friendship of Nuno Castro and Filipe Veloso along this work. They were always available to help me out on a wide range of problems since the beggining.

I warmly thank Professor Juan Antonio Aguilar Saavedra for providing the theoretical background of this work and for his high-yield collaboration. I also thank Professor Orlando Oliveira for the suggestions given in the Theoretical Framework chapter of this thesis.

I thank to all my office and working colleagues, in particular, to Inês Firmo and Matilde Castanheira for their true friendship and back-up. To my long term friends, Filipe, Rui, Miguel, JP, Jorge, Tiago and Pedro, my deepful thanks for their presence and support in the good and not so good moments.

I also thank Professors José António Paixão and Fernando Nogueira for teaching me the art and craft of problem solving in physics. Their passion and dedication to olympic leadership is responsible for a whole new generation of young portuguese physicists in which I am included.

Finally, I thank my family and Susana for their affection and for enduring me for so long.

I acknowledge the support given by Fundação para a Ciência e Tecnologia, through the projects POCI/FP/63420/2005, POCI/FP/63926/2005, POCI/FP/81950/2007 and GRID/GRI/81727/2006.

Contents

List of Figures

List of Tables

Chapter 1

Introduction

The top quark can be produced at the LHC by two main mechanisms, pair production ($t\bar{t}$) and single production (single top) via the strong and weak interactions, respectively. The single top production mechanism has a lower cross section, in three different channels: the t-channel, Wt production and s-channel. While the $t\bar{t}$ process was first observed at the Fermilab by the CDF and D0 experiments in 1995 [1, 2], single top (t+s channels) was only observed in December 2006 by the D0 experiment [3]. Due to the low statistics available in these experiments, no measurements besides the cross sections were yet made in the single top channels. In the Large Hadron Collider (LHC), with an integrated luminosity of 10 fb^{-1} per year and per experiment (in the low luminosity phase) and a centre of mass energy of $\sqrt{s} = 14\,\text{TeV}$, the amount of statistics available will be much larger, which will allow to determine the top quark properties with higher precision.

In this thesis, the leptonic t-channel single top quark production was studied. A sequential analysis and a discriminant analysis were developed to select signal events and eliminate the background contamination as much as possible. After the analysis, several observables, such as angular and spin asymmetries, were determined in order to study the W boson and top quark polarizations in the $t \to Wb$ vertex. The statistical and systematical uncertainties for these observables were determined and used to calculate the limits at 68.3% CL and 10 fb^{-1} on the anomalous couplings that may appear at the Wtb vertex using the TopFit library [4, 5].

The structure of this thesis is as follows. In the second chapter, the Standard Model and the top quark are introduced, the top quark properties and its production mechanisms are discussed, mostly for the single top channel. In the third chapter, the CERN and the Large Hadron Collider are briefly presented. It is also included a detailed description of the ATLAS detector and an overview of the detector performance. In the fourth chapter, the generation and the simulation of events used in the analysis are presented. A detailed description of the sequential and probabilistic selection of events is shown in the fifth chapter. The results for the angular and spin asymmetries, and the respective statistical and systematical uncertainties, are presented in the sixth chapter, as well as the limits on the anomalous couplings. The last chapter is left to the conclusions and comments about this study.

Chapter 2

Theoretical Framework

In this chapter, the Standard Model is briefly discussed: the properties of the top quark, its mechanisms of production at the LHC and, in particular, the single top channel. The latest experimental results on single top quark production are also presented.

2.1 The Standard Model

The Standard Model is a $SU(3)_c \times SU(2)_L \times U(1)_Y$ Relativistic Quantum Field Theory unifying the electromagnetic, weak and strong interactions. According to the Standard Model, matter is divided in fermions and bosons.

The fermions are spin $\frac{1}{2}$ particles obeying the Pauli Exclusion Principle. A total of twelve fermions are known, apart from the antiparticle partners, and are classified as quarks (up, down, charm, strange, top, bottom) and leptons (electron, muon, tau, and their corresponding neutrinos). Quarks interact via the strong, electromagnetic and weak forces since they hold color charge, electric charge and weak isospin. This class of particles can also form color-neutral particles, the hadrons, which are divided into baryons (three quarks) and mesons (quark-antiquark systems). Leptons have zero color charge, therefore, only interact through the electroweak force. In particular, neutrinos do not have electric charge as well, therefore, can only interact via the weak interaction.

In the Standard Model, all force mediating particles have spin 1. These

particles are gauge bosons and are divided into three kinds: photons, massive bosons and gluons. The photons are massless particles and mediate the electromagnetic interaction. The massive gauge bosons are the W^+, W^- and Z particles. Together with the photons, these particles are part of the electroweak interaction, the unification of electromagnetism and weak interaction on a single description. The Z boson is electrically neutral and more massive than the W bosons ($m_W = 80.398 \pm 0.25\text{GeV/c}^2$ and $m_Z = 91.1876 \pm 0.0021\text{GeV/c}^2$) [6]. Finally, there are eight different gluons that mediate the strong force. According to quantum chromodynamics, gluons are massless and color charged particles, therefore, they can interact among themselves.

The Standard Model Lagrangian includes the quantum chromodynamics and the electroweak interactions:

$$\mathcal{L}_{SM} = \mathcal{L}_{QCD} + \mathcal{L}_{electroweak} \tag{2.1}$$

The electroweak interaction is described in the Weinberg-Salam-Glashow model [7]. The unification of electromagnetic and weak forces is achieved under a $SU(2)_L \times U(1)_Y$ gauge group where the hypercharge operator $\hat{Y}$ is the generator of $U(1)$ and the generator of $SU(2)$ is the weak isospin operator $\hat{T}$. The electric charge is related with the hypercharge (Y) and the third component of weak isopsin (T_3) as:

$$Q = \frac{1}{2}Y + T_3. \tag{2.2}$$

The left-handed leptons and quarks are organized in $SU(2)_L$ doublets:

$$\begin{pmatrix} \nu_e \\ e \end{pmatrix}_L \begin{pmatrix} \nu_\mu \\ \mu \end{pmatrix}_L \begin{pmatrix} \nu_\tau \\ \tau \end{pmatrix}_L \tag{2.3}$$

$$\begin{pmatrix} u \\ d' \end{pmatrix}_L \begin{pmatrix} c \\ s' \end{pmatrix}_L \begin{pmatrix} t \\ b' \end{pmatrix}_L \tag{2.4}$$

with the corresponding right-handed fields transforming as singlets under $SU(2)_L$. The electroweak charges Q, Y and the third component of weak isopsin (T_3) for quarks and leptons in the Standard Model are collected on Table 2.1.

	ν_L^e	e_L^-	e_R^-	u_L	d_L	u_R	d_R
Q	0	-1	-1	2/3	-1/3	2/3	-1/3
T_3	1/2	-1/2	0	1/2	-1/2	0	0
Y	-1	-1	-2	1/3	1/3	4/3	-2/3

Table 2.1: *Electroweak charges Q, Y and the third component of the weak isospin T_3 for quarks and leptons in the Standard Model.*

The Lagrangian density for the electroweak interaction is divided in three parts:

$$\mathcal{L}_{electroweak} = \mathcal{L}_{gauge} + \mathcal{L}_{fermions} + \mathcal{L}_{Higgs}. \tag{2.5}$$

The kinetic and self interacting gauge fields component is given by:

$$\mathcal{L}_{gauge} = -\overbrace{\frac{1}{4}F_i^{\mu\nu}F_{\mu\nu}^i}^{SU(2)} - \overbrace{\frac{1}{4}B^{\mu\nu}B_{\mu\nu}}^{U(1)}, \tag{2.6}$$

with

$$F_{\mu\nu}^i = \partial_\mu W_\nu^i - \partial_\nu W_\mu^i - g_2\epsilon^{ijk}W_\mu^j W_\nu^k, \tag{2.7}$$

$$B_{\mu\nu} = \partial_\mu B_\nu - \partial_\nu B_\mu. \tag{2.8}$$

where $\vec{W}_\nu$ is the three-component $SU(2)$ gauge field and B_ν is the $U(1)$ gauge field. The fermionic part is defined as:

$$\mathcal{L}_{fermions} = \sum_{\psi_L} \bar{\psi}_L \mathrm{i}\not{D}\psi_L + \sum_{\psi_R} \bar{\psi}_R \mathrm{i}\not{D}\psi_R. \tag{2.9}$$

with

$$\mathcal{D}_\mu\psi_R = \left(\partial_\mu + \frac{\mathrm{i}}{2}g_1 Y B_\mu\right)\psi_R, \tag{2.10}$$

$$\mathcal{D}_\mu\psi_L = \left(\partial_\mu + \frac{\mathrm{i}}{2}g_1 Y B_\mu + \frac{\mathrm{i}}{2}g_2\vec{\tau}\cdot\vec{W}_\mu\right)\psi_L, \tag{2.11}$$

where $\vec{\tau}$ are the Pauli matrices. Furthermore, g_1 and g_2 are the electroweak couplings for the $U(1)_Y$ and $SU(2)_L$ groups, respectively.

The Higgs Lagrangian term $\mathcal{L}_{Higgs}$ contains the Higgs potential and the kinetic terms of the Higgs field. The Higgs field has a non-zero vacuum expectation value which spontaneously breaks electroweak symmetry. Such mechanism to giving mass to the gauge bosons is often referred in the literature as the Higgs mechanism.

The gauge invariant Lagrangian density for the strong interaction, which describes the dynamics of quarks and gluons, is given by:

$$\begin{aligned}\mathcal{L}_{QCD} &= \bar{\psi}_i(\mathrm{i}\gamma^\mu(D_\mu)_{ij} - m\delta_{ij})\psi_j - \frac{1}{4}G^a_{\mu\nu}G^{\mu\nu}_a \\ &= \bar{\psi}_i(\mathrm{i}\gamma^\mu\partial_\mu - m)\psi_i - gG^a_\mu\bar{\psi}_i\gamma^\mu T^a_{ij}\psi_j - \frac{1}{4}G^a_{\mu\nu}G^{\mu\nu}_a \qquad (2.12)\end{aligned}$$

where T^a are the $SU(3)$ color generators, the ψ_j are the quarks fields and $G^a_\mu(x)$ are the gluon fields. The Dirac matrices and coupling constant are given by γ^μ and g_s, respectively. The gluon field tensor is represented by:

$$G^a_{\mu\nu} = \partial_\mu G^a_\nu - \partial_\nu G^a_\mu - gf^{abc}G^b_\mu G^c_\mu \qquad (2.13)$$

2.1.1 CKM matrix

The Cabibbo-Kobayashi-Maskawa mixing matrix is an unitary matrix with four independent parameters which contains information of flavour-changing weak decays. The CKM matrix in the parameterization of Kobayashi and Maskawa uses three angles (θ_1, θ_2, θ_3) and a CP-violating phase (δ). The cosines and sines of the angles are denoted c_i and s_i, respectively:

$$\begin{bmatrix} c_1 & -s_1c_3 & -s_1s_3 \\ s_1c_2 & c_1c_2c_3 - s_2s_3e^{i\delta} & c_1c_2s_3 + s_2c_3e^{i\delta} \\ s_1s_2 & c_1s_2c_3 + c_2s_3e^{i\delta} & c_1s_2s_3 - c_2c_3e^{i\delta} \end{bmatrix}$$

According to the Particle Data Group, the CKM matrix element amplitudes take the following form [6] assuming unitarity and three families of quarks:

$$V \equiv \begin{pmatrix} V_{ud} & V_{us} & V_{ub} \\ V_{cd} & V_{cs} & V_{cb} \\ V_{td} & V_{ts} & V_{tb} \end{pmatrix}$$

$$= \begin{pmatrix} 0.97383^{+0.00024}_{-0.00023} & 0.2272^{+0.0010}_{-0.0010} & (3.96^{+0.09}_{-0.09}) \times 10^{-3} \\ 0.2271^{+0.0010}_{-0.0010} & 0.97296^{+0.00024}_{-0.0024} & (42.21^{+0.10}_{-0.80}) \times 10^{-3} \\ (8.14^{+0.32}_{-0.64}) \times 10^{-3} & (41.61^{+0.12}_{-0.78}) \times 10^{-3} & 0.999100^{+0.000034}_{-0.000004} \end{pmatrix} \quad (2.14)$$

Each CKM matrix element contains the information about the probability of a transition from one quark q to another quark q' in the vertex $q \to q'W^{\pm}$. For example, the $t \to Wb$ vertex transition probability is proportional, in first order, to $|V_{tb}|^2$. Since V_{td} and V_{ts} are much smaller than V_{tb}, the top quark decays mainly to a W boson and bottom quark. The constraints of unitarity of the CKM-matrix imply that the sum of all couplings of any of the up-type quarks to all the down-type quarks is the same for all generations. This relation is called weak universality. Kobayashi and Maskawa shared one half of the 2008 Nobel Prize in Physics "for the discovery of the origin of the broken symmetry which predicts the existence of at least three families of quarks in nature".

2.2 Top quark

The top quark is the third-generation up-type quark and it was the last to be discovered, in 1995, by the CDF and D0 experiments [1, 2] at Fermilab. The top quark has a mass of $172.6 \pm 1.4\,\mathrm{GeV/c^2}$ [8], which is about the gold atom nucleus mass, and an electric charge of $+2/3\ |e|$. It can only decay through the weak force, and dominantly to a W boson and a bottom quark, with a mean lifetime of $10^{-25}\,\mathrm{s}$, much shorter than the mean hadronization time ($10^{-24}\,\mathrm{s}$). Since the top quark is the only quark able to decay before the hadronization takes place, it allows to study its properties with unprecedent accuracy.

The top quark can be produced by two main mechanisms at the LHC, pair production ($t\bar{t}$) and single production (single top) via the strong and weak interactions, respectively. At the LHC, the $t\bar{t}$ production will be dominated by the processes $q\bar{q} \to t\bar{t}$ and $gg \to t\bar{t}$ with a cross section of $833^{+52}_{-39}\,\mathrm{pb}$ [9] assuming the Standard Model at NLO (Next to Leading Order). The single top is produced in three different processes: the t-channel, the s-channel and associate production. The single production is less probable than the $t\bar{t}$ process. The expected cross sections are $246^{+11.8}_{-12.2}\,\mathrm{pb}$ for the t-channel,

$10.65^{+1.12}_{-1.02}$ pb for the s-channel [10] and 66 ± 2 pb for the associate production [11]. The $t\bar{t}$ process was first observed at the Fermilab by the CDF and D0 experiments in 1995 while the single top (t+s channels) was observed in December 2006 at D0 experiment with a three sigma evidence.

The top quark decays under the weak interaction mostly to a W boson and a bottom quark. In fact, the branching ratio of the $t \to Wb$ process is proportional to $|V_{tb}|^2$ in first order. For the vertices $t \to Ws$ and $t \to Wd$, the CKM matrix elements are much lower, therefore, these processes are less probable to occur. The width of the $t \to Wb$ vertex is given, at Leading Order (LO), by:

$$\Gamma_{LO}(t \to Wb) = \frac{G_F m^3}{8\pi\sqrt{2}} |V_{tb}|^2 m_t^3 \Big(1 - 3\frac{M_W^4}{m_t^4} + 2\frac{M_W^6}{m_t^6}\Big), \tag{2.15}$$

where m_t and m_W are the top and the W boson masses, respectively. The result for the width using the experimental mass values is $\Gamma_{LO} = 1.56\,\text{GeV}$ and $\Gamma = 1.42\,\text{GeV}$ [12] taking into account higher order corrections.

2.3 Single top quark production

2.3.1 Single top t-channel

The single top processes, t-channel, s-channel and associate production are shown in Figure 2.1, in particular, the t-channel and s-channel single top quarks are produced via weak interactions. The top quark decays mostly to a W boson and a bottom quark while the W boson can decay leptonically or hadronically. Therefore, the single top t-channel was divided in three different final state topologies:

- **Hadronic sample**: The W boson decays to a pair of quarks with a branching ratio of $67.60 \pm 0.27\%$. The final topology is $qb \to q't \to q'Wb \to q'jjb$.

- **Leptonic sample without taus**: The W boson decays to an electron or a muon and the respective neutrino with a branching ratio of $21.60 \pm 0.13\%$. The final topology is $qb \to q't \to q'Wb \to q'l\nu_l b$, with $l = e, \mu$.

- **Leptonic sample with taus**: The W boson decays to a tau and the respective neutrino with a branching ratio of $10.80 \pm 0.09\%$. Furthermore, the tau lepton decays dominantly to a pair of jets. The final topology is $qb \rightarrow q't \rightarrow q'Wb \rightarrow q'\tau\nu_\tau b$

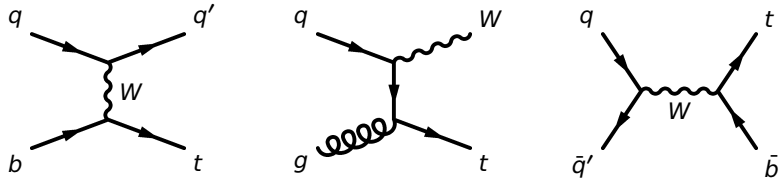

Figure 2.1: *Single top production examples (t-channel, associate production and s-channel).*

A more detailed Feynman diagram of the leptonic t-channel single top is shown in Figure 5.1. It is visible the presence of an extra bottom quark. However, this quark flies at low angle making very hard to be tagged as a b jet by the detector.

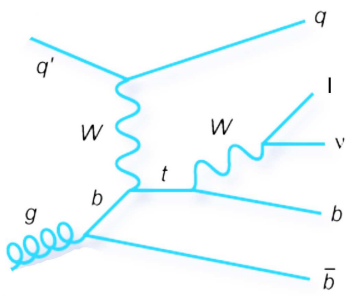

Figure 2.2: *Leptonic single top t-channel.*

Furthermore, the measurement of the t-channel cross section allows the evaluation of the V_{tb} and, therefore, will provide a better understanding of the Standard Model.

2.3.2 Anomalous couplings

The most general on-shell Wtb vertex Lagrangian with terms up to dimension five [4] is given by:

$$\mathcal{L} = -\frac{g}{\sqrt{2}}\bar{b}\gamma^{\mu}(V_L P_L + V_R P_R)tW_{\mu}^{-} - \frac{g}{\sqrt{2}}\bar{b}\frac{i\sigma^{\mu\nu}q_{\nu}}{M_W}(g_L P_L + g_R P_R)tW_{\mu}^{-} + h.c. \tag{2.16}$$

with $q = p_t - p_b$ the W boson momentum. In the Standard Model, $V_L = V_{tb} \approx 1$ and the anomalous couplings, V_R, g_R and g_L vanish at the tree level [13]. These couplings can be related with the W boson helicity fractions and can be taken as real numbers if CP conservation is assumed. According to some models beyond the Standard Model, these anomalous coupling may experience contributions of new physics. Since the W boson helicity fractions are related to these anomalous couplings, the measurement of these observables is important to search for evidence of new physics. The dependence of the helicity fractions and angular aymmetries on the anomalous couplings is shown in Figures 2.5 and 2.6 [4].

The spin asymmetries are less sensitive to new physics in the Wtb vertex but may be sensitive to new physics in the top quark production. Therefore, the correct strategy is to set constraints on the Wtb vertex anomalous couplings by measuring the angular asymmetries and then use this information to look for new physics through the spin asymmetries [5].

2.3.3 Angular asymmetries and W boson polarization

In the $t \to Wb$ vertex, the W boson may hold three different helicity states: longitudinal, left-handed and right-handed. According to the Standard Model, the top quark decays to a longitudinally polarized W boson with a probability of 70.3%, at leading order. The left-handed and right-handed W boson helicity states fractions are 29.7% and 0.036%, respectively [4]. The right-handed polarization of the W boson is almost absent because it forces the bottom quark to be right-handed which is very unlikely to occur due to its low mass. An angular distribution, defined as the angle between the lepton and the bottom quark in the W boson rest frame, θ_l, allows to study the W

boson polarization. The angle used is, in fact, the supplementary, $\theta_l^* = \pi - \theta_l$. The normalized angular distribution for the charged lepton is given by [4]:

$$\frac{1}{\Gamma}\frac{\mathrm{d}\Gamma}{\mathrm{d}\cos\theta_\ell^*} = \frac{3}{4}\sin^2\theta_\ell^*\, F_0 + \frac{3}{8}(1-\cos\theta_\ell^*)^2\, F_L + \frac{3}{8}(1+\cos\theta_\ell^*)^2\, F_R \qquad (2.17)$$

where F_0, F_L and F_R are the fractions of the longitudinal, left-handed and right-handed helicities, respectively. Since the right-handed helicity fraction is much lower than the others, the Standard Model distribution, shown in Figure 2.3, depends mainly on the longitudinal and left-handed helicities contributions.

From this distribution, a set of angular asymmetries, sensitive to the anomalous couplings, are defined as:

$$A_z = \frac{N(\cos\theta_\ell^* > z) - N(\cos\theta_\ell^* < z)}{N(\cos\theta_\ell^* > z) + N(\cos\theta_\ell^* < z)} \qquad (2.18)$$

$$z = 0 \;\rightarrow\; A_{FB} = \frac{3}{4}(F_R - F_L) = -0.223$$

$$z = -(2^{2/3}-1) \;\rightarrow\; A_+ = 3\beta[F_0 + (1+\beta)F_R] = 0.548$$

$$z = (2^{2/3}-1) \;\rightarrow\; A_- = -3\beta[F_0 + (1+\beta)F_L] = -0.840$$

where N is the number of events and $\beta = (2^{2/3}-1)$. The values of these observables were calculated with the Standard Model distribution at leading order. The forward-backward asymmetry, A_{FB}, is insensitive to the longitudinal fraction while the A_+ and A_- are not sensitive to the left-handed and right-handed helicities, respectively.

2.3.4 Spin asymmetries and top polarization

According to the Standard Model at leading order, the top quark is mostly left-handed in the single top quark production. In the single top t-channel, a set of angular distributions from the top decay, θ_X, sensitive to the anomalous couplings, are defined using the angle between the $X = l, \nu, b$ particle and

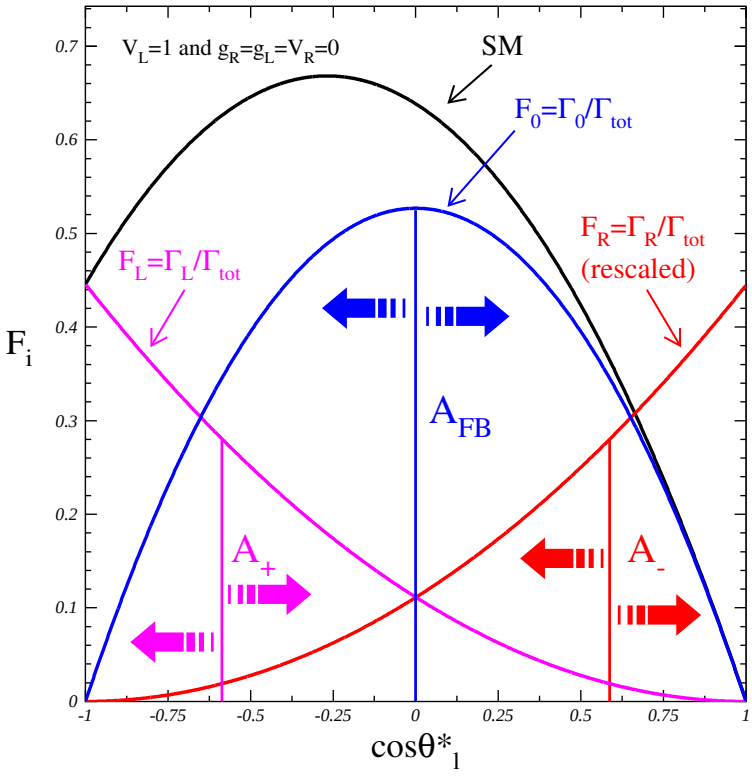

Figure 2.3: *Angular distributions and asymmetries representation on the Wtb vertex.*

the non-b jet in the Top rest frame. These distributions, which are used to study the top quark polarization, are given by [4]:

$$\frac{1}{\Gamma}\frac{\mathrm{d}\Gamma}{\mathrm{d}\cos\theta_X} = \frac{1}{2}(1 + P\alpha_X \cos\theta_X) \tag{2.19}$$

where P is the top polarization, which is approximately 0.89 [14]. The constants α_X are called "spin analysing power" of X and, in the Standard Model, $\alpha_l = 1$, $\alpha_\nu = -0.319$ and $\alpha_b = -0.406$ at the tree level. The Standard Model distributions at leading order are shown in Figure 2.4. For each spin analyzer, the spin asymmetries are defined as:

$$A_X = \frac{N(\cos\theta_X > 0) - N(\cos\theta_X < 0)}{N(\cos\theta_X > 0) + N(\cos\theta_X < 0)} = \frac{1}{2}P\alpha_X \tag{2.20}$$

In the Standard Model, at leading order, the spin asymmetries and their ratios take the following values:

$$
\begin{aligned}
A_l &= 0.445 \\
A_\nu &= -0.142 \\
A_b &= -0.181 \\
r_{\nu l} &= \frac{A_\nu}{A_l} = -0.319 \\
r_{bl} &= \frac{A_b}{A_l} = -0.406
\end{aligned}
$$

The distributions are the same for the particles and antiparticles since $\alpha_X = -\alpha_{\bar{X}}$, as long as CP is conserved in top quark decays.

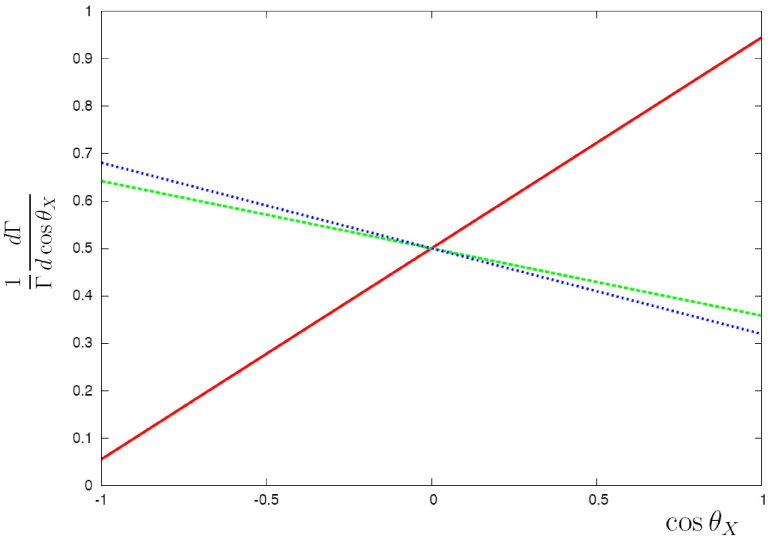

Figure 2.4: *Spin distributions of the top decay for the lepton (red), neutrino (green), b-jet (blue).*

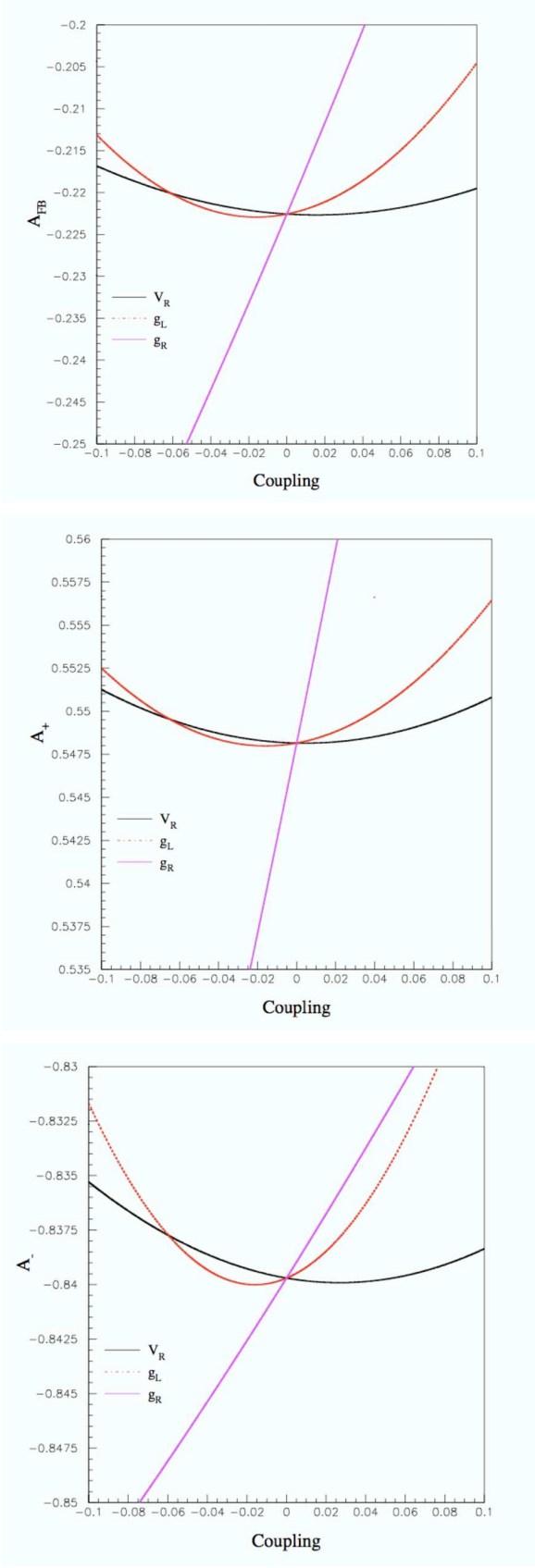

Figure 2.5: *Angular asymmetries dependence on the anomalous couplings:* A_{FB}, A_+ *and* A_-

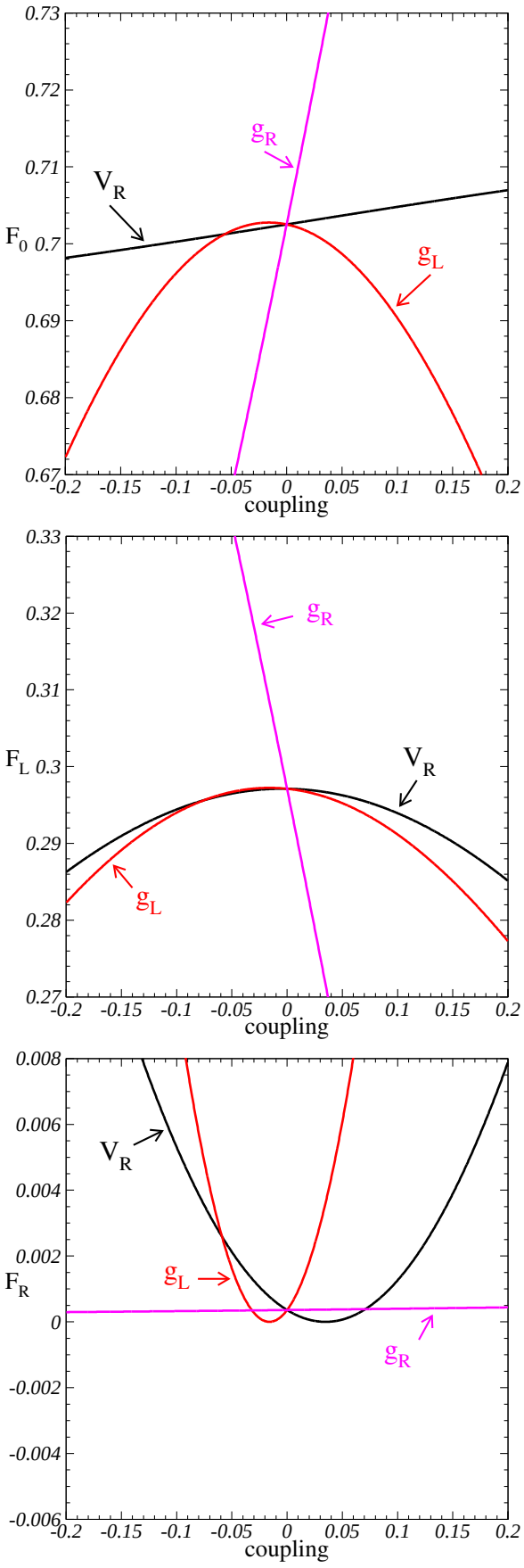

Figure 2.6: *Helicity fractions dependence on the anomalous couplings: F_0, F_L and F_R*

Chapter 3

ATLAS Detector

In this chapter, the CERN laboratory and the Large Hadron Collider are briefly presented as well as a short description of the ATLAS detector and an overview of the detector performance.

3.1 CERN

The European Organization for Nuclear Research (CERN), located on the french-swiss border is the largest scientific laboratory of the world. There are 20 state-members and since its beginning, in 1954, it has given an huge contribution for science and technology. Several scientific discoveries and technological advances took place on CERN.

3.2 LHC

The Large Hadron Collider (LHC) is a particle accelerator located at CERN. The circular tunnel, built for the previous collider, the Large Electron-Positron Collider (LEP), is 27km long and is placed 50-175 meters underground. Thousands of scientists and engineers are linked to the LHC and the first beams were injected in September 2008.

In this collider, protons will be accelerated to a nominal energy of 7 TeV along the beam pipe. Therefore, the energy in the pp rest frame will be $\sqrt{s} = 14\,\text{TeV}$. Since the protons will travel at 99.999 % of the speed of

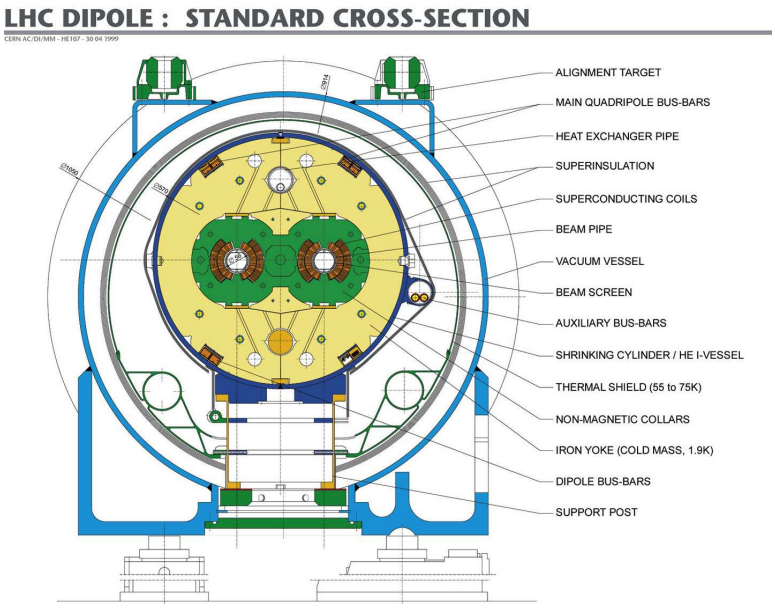

Figure 3.1: *Dipole System of the LHC.*

light, large magnetic fields are required to bend the beam, which can only be achieved by low temperature superconducting magnets. At 7 TeV, each of the 2808 bunches will take 90 μs to complete the circular perimeter and each bunch will be spaced by 7.48 m. The total cross-section for proton-proton collisions at this energy will be around 110 mb.

At the LHC, the superconducting magnets of Nb-Ti (Niobium-Titanium) will produce magnetic fields of about 8 T at a temperature under 2 K. There are 1232 superconducting main dipoles, each 14.3 meters long, to bend the beam and 400 superconducting main quadrupoles to focus the beam. These main dipoles have two pipes, so that the beam can flow on opposite directions, and must operate at 8.33 T with electric currents of 11700 A at 7 TeV. Due to the high heat conduction of He II, the cryogenic system will use superfluid helium at 1.9 K to increase these superconductors performance [15]. A transverse view of the pipe is shown in Figure 3.1 where the two pipes of the beam can be seen as well as the superconducting coils around.

The Large Hadron Collider will hold four main experiments, the A Toroidal LHC ApparatuS (ATLAS), the Compact Muon Solenoid (CMS), the A Large

Ion Collider Experiment (ALICE) and LHCb, with four collision points in total, one for each main detector. In Figure 3.2 it is shown the LHC circular pipe divided into eight octants and the main experiments.

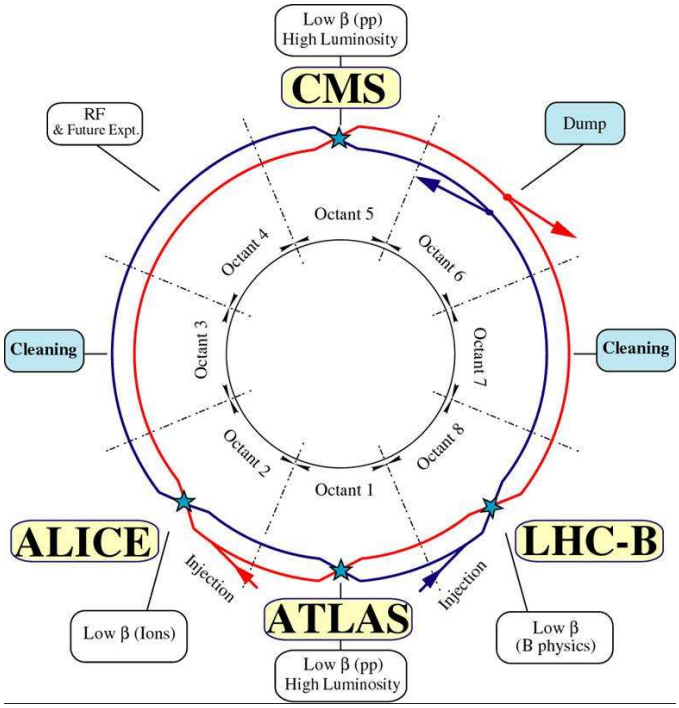

Figure 3.2: *The LHC in scheme*

3.3 ATLAS

The ATLAS detector [16] is a general purpose detector at the LHC. The detector is 46 metres long, 25 metres in diameter and weighs about 7000 tonnes. It is expected to discover, for instance, the Higgs boson or another mechanism of electroweak symmetry breaking. In this experiment it will be possible to identify and measure the momentum, energy and electric charge of all stable particles produced at the interaction point (but not for the neutrino).

ATLAS has several layers, each with a specific purpose on the reconstruction of particles. The four main components are the Inner Detector, the

calorimeters, the muon spectrometer and the magnetic systems. The Inner Detector is placed near the beam pipe and it is intended to record the first hits of charged particles that interact with the detector material. There is also a solenoid around the Inner Detector that creates a 2 T magnetic field, which is strong enough to curve very energetic particles, leading to the measurement of their momentum. The hadronic and electromagnetic calorimeters are in the layer surrounding the Inner Detector, both with the basic function of measuring the particles energies. The electromagnetic calorimeter was designed to measure the energy of charged particles and photons through the electromagnetic interaction, while the hadronic calorimeter measures the energy of hadrons that interact via the strong interaction. The muon spectrometer starts at a radius of 4.25 m around the calorimeters and extends to the end of the detector, a radius of 11 m. Like in the Inner Detector, the momentum of the muons is computed from the deflection of their trajectories in the magnetic field. There are two magnetic systems, a solenoid surrounding the Inner Detector and the toroid magnets. The toroid magnets surround the calorimeters and generate the magnetic field for the muon spectrometer. All these components will be described with more detail in the following subsections.

The pseudo-rapidity is an important variable in ATLAS and is defined as $\eta = -\ln\tan(\theta/2)$ where θ is the polar angle, the angle between the object momentum and the beam pipe (z-axis), while the azimuthal angle is represented by ϕ. Another important variable is the momentum in the transverse plane defined as $p_T = \sqrt{p_x^2 + p_y^2}$. The positive x-axis is defined as pointing from the interaction point to the centre of the LHC ring and the positive y-axis is defined as pointing upwards.

To achieve its goals there are a set of requirements for the detector [16]:

- Fast electronics, resistant to the radiation, and high granularity to reduce events overlap.
- Large acceptance in pseudorapidity with a very large coverage in the azimuthal angle.
- Good resolution in the charged particles momentum and reconstruction efficiency in the Inner Detector. Pixel detectors close to the interaction

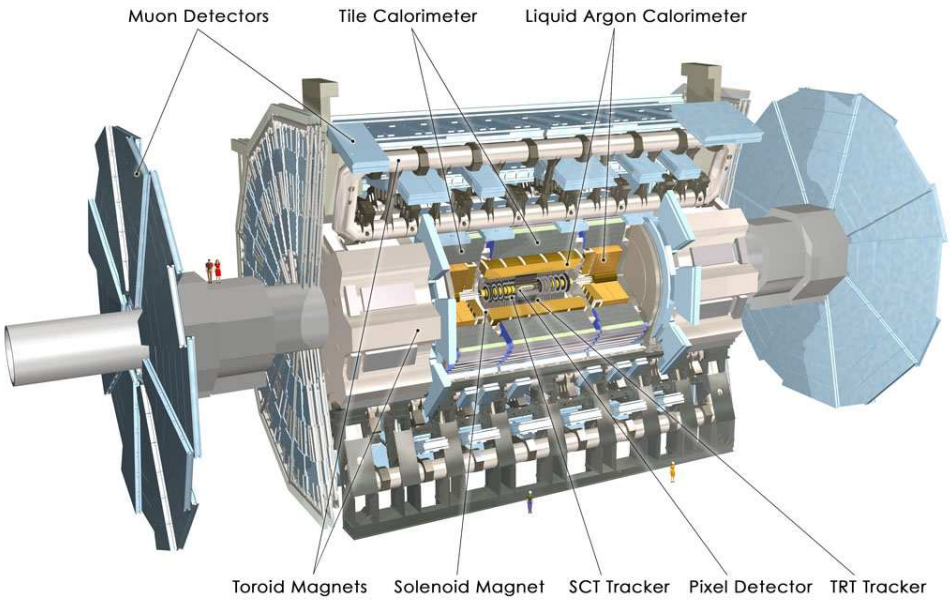

Figure 3.3: *ATLAS detector scheme.*

point are required for an efficient triggering and offline tagging of τ's and b-jets by observation of secondary vertices.

- An electromagnetic calorimeter with a large power of identification and measurement of photons and electrons and an accurate hadronic calorimeter to measure jet and missing transverse energy with precision.

- An independent muon identification with good momentum resolution to determine unambiguously the charge of high p_T muons.

- A triggering system for low p_T particles with sufficient background rejection to allow the observation of most physics processes of interest at the LHC.

The structure of the detector is shown on Figure 3.3 and the general performance goals of the ATLAS detector are on Table 3.1 [16].

Component	Resolution	η	*Trigger* (η)
ID	$\frac{\sigma_{p_T}}{p_T} = 0.05\% p_T \oplus 1\%$	± 2.5	
EM Cal.	$\frac{\sigma_E}{E} = 10\%/\sqrt{E} \oplus 0.7\%$	± 3.2	± 2.5
Hadronic Cal.			
barrel and end-cap	$\frac{\sigma_E}{E} = 50\%/\sqrt{E} \oplus 3\%$	± 3.2	± 3.2
forward	$\frac{\sigma_E}{E} = 100\%/\sqrt{E} \oplus 10\%$	$3.1 < \lvert\eta\rvert < 4.9$	$3.1 < \lvert\eta\rvert < 4.9$
Muon detection	$\frac{\sigma_{p_T}}{p_T} = 10\%$ at p_T=1 TeV	± 2.7	± 2.4

Table 3.1: *General detector performance.*

3.3.1 Inner Detector

The Inner Detector, dedicated to the tracking and identification of charged particles, is the closest layer to the beam pipe, beggining only a few centimeters away from it. It is seven metres long and extends to a radius of 1.2 m. The Inner Detector has three parts, the Pixel Detector, the Semiconductor Tracker (SCT) and the Transition Radiation Tracker (TRT), all contained on the 2 T magnetic field to measure the particles momenta. The Pixel Detector is the innermost part of detector and consists of 3 cylindrical layers composed by pixel sensors and microstrips. Due to its location, the Pixel Detector must be very resistant to radiation. The Semiconductor Tracker is very similar to the Pixel Detector but measures particles over a much larger area, therefore, it is useful for tracking in the plane perpendicular to the beam. The Transition Radiation Tracker is a combination of a straw tracker formed by many small straws and a transition radiation detector providing about 36 points per track. The TRT also identifies electrons by the detection of transition-radiation photons in the xenon gas mixture of the straw tubes. The combination of the two techniques provides a very robust pattern recognition and high precision in the azimuthal angle, ϕ, and in the z coordinate.

The Inner Detector provides high resolution in momentum and full tracking coverage over $|\eta| < 2.5$ above the p_T threshold. The ATLAS Inner Detector is shown in Figure 3.4.

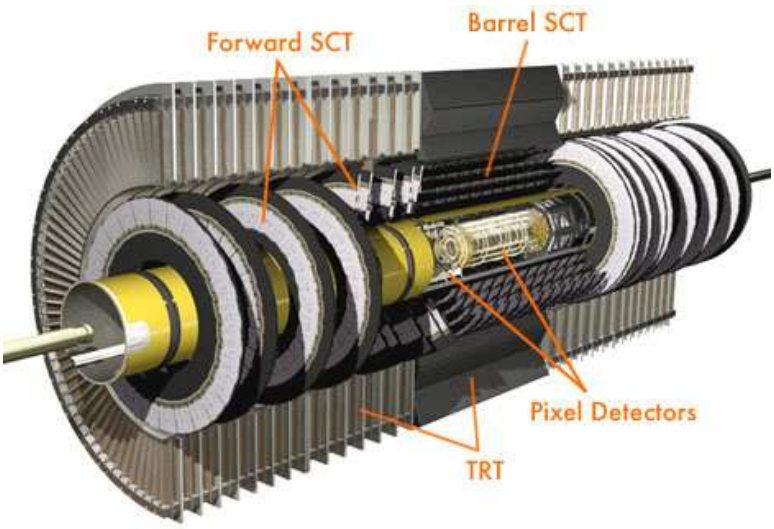

Figure 3.4: *The Inner Detector scheme.*

3.3.2 Magnet System

The ATLAS magnetic system has 22 metres in diameter and is 26 metres long with an overall stored energy of 1.6 GJ. This magnet system is formed by four superconducting magnets, the inner solenoid which provides a 2 T magnetic field parallel to the beam pipe for the inner detector, the barrel toroid and the two end-cap toroids that create a toroidal magnetic field between 0.5 T and 1 T for the muon spectrometer.

The solenoid has an inner radius of 2.46 m, an outer radius of 2.63 m and is 5.29 m long, with a stored energy of 39 MJ. The nearly uniform magnetic field produced by this solenoid is strong enough to bend very energetic particles. Due to the strong magnetic field, the detector system will not be able to measure the momentum of low energy particles (hundreds of MeV).

The barrel toroid is formed by eight coils, shown in Figure 3.5, installed in a lenght of 25.3 m with an inner radius of 9.4 m and an outer radius of 20.1 m, involving the calorimeters. The two-end cap toroids are necessary to increase the magnetic field in the end cap region. These end-cap toroids weight 240 tons and will be subject to a Lorentz force of 280 tons pushing them into the barrel toroid. The barrel toroid and the two end-caps do not

produce an uniform magnetic field in the muon spectrometer.

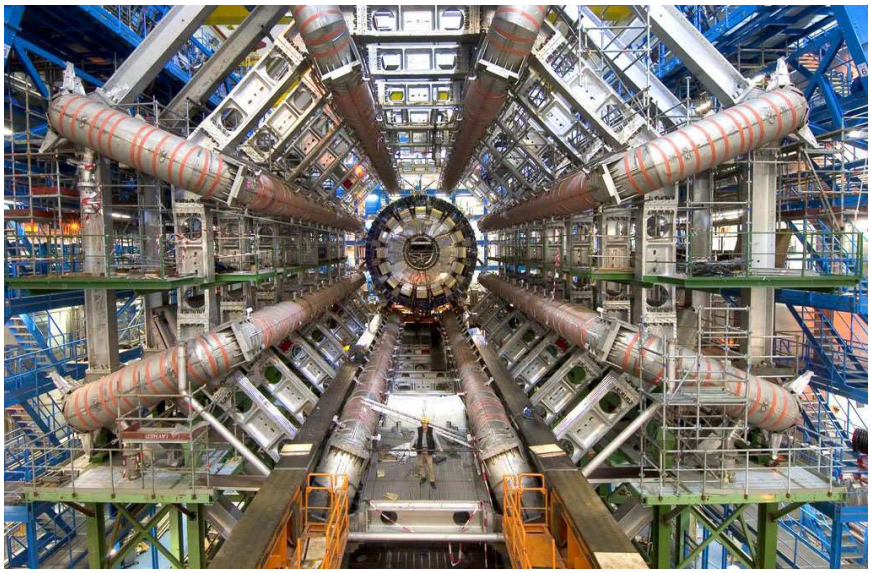

Figure 3.5: *Barrel Toroid*

3.3.3 Calorimeters

There are two calorimeters in the ATLAS detector, the electromagnetic and the hadronic, covering the regions $|\eta| < 3.2$ and $|\eta| < 4.9$, respectively. The electromagnetic calorimeter was designed to identify and measure the energy of the particles that interact through the electromagnetic force. The hadronic calorimeter will absorb the energy of particles that interact through the strong force, after crossing the electromagnetic calorimeter. The hadronic calorimeter is meant to detect the particle shower resulting from the hadronization of the quarks, also known as jet, allowing to measure the energy of the original particle after a calibration.

The electromagnetic calorimeter [17] is a lead/liquid-argon detector with accordion geometry that provides full azimuthal symmetry. The electromagnetic calorimeter is divided into a barrel part ($|\eta| < 1.475$) and two end-caps ($1.375 < |\eta| < 3.2$). The central barrel is divided in two half barrels and the two end-caps are divided in two coaxial wheels. The outer and inner

wheels cover the regions ($1.375 < |\eta| < 2.5$) and ($2.5 < |\eta| < 3.2$), respectively. In order to recover information about the energy loss along the way to the calorimeter, there is a liquid-argon layer before the electromagnetic calorimeter.

The hadronic calorimeter [17] is formed by three kinds of hadronic calorimeters, the TileCal (Tile Calorimeter), the HEC (Hadronic End-Cap) and the FCal (Forward Calorimeter). The TileCal covers the region $|\eta| < 1.7$ and extends from an inner radius of 2.28 m to an outer radius of 4.25 m. It is composed by one barrel and two extended barrels, each with 64 modules, covering the regions $|\eta| < 1.0$ and $0.8 < |\eta| < 1.7$, respectively. The HEC covers the region $1.5 < |\eta| < 3.2$ overlapping the forward calorimeter. Each HEC consists of two wheels with a radius of 2.03 m, each with 32 modules and is divided in two longitudinal segments. Finally, the FCal is located at 4.5 m from the interaction point covering the region $3.1 < |\eta| < 4.9$ with the main purpose of minimising the loss of energy and reduce background radiation levels in the muon spectrometer. The TileCal is composed by iron as the absorver and scintillating tiles as the active material while FCal and HEC use cooper as the absorver and LAr as the active material.

3.3.4 Muon System

The muon spectrometer is based on the magnetic deflection of muon tracks and extends from a radius of 4.25 m around the calorimeters to the outer radius of the detector. Despite the different magnetic field configuration and lower spatial precision, the muon spectrometer works under the same base of the inner detector, with muons curving in the magnetic field allowing the measurement of their momentum.

The magnetic bending is provided by the barrel toroid and by two end-cap magnets in the regions $|\eta| < 1.0$ and $1.0 < |\eta| < 1.4$, respectively. To efficiently identify and measure muons, the Muon Spectrometer is composed by four different tracking detector technologies: Monitored Drift Tubes (MDT) and Cathode Strip Chambers (CSC) precision detectors in the barrel and endcap regions; Resistive Plate Chambers (RPC) and Thin Gap Chambers (TGC) that provide fast trigger signals in the barrel and endcap regions.

3.3.5 Trigger and data acquisition system

In the LHC there will be a rate of 10^9 interactions per second that will create 1 Petabyte/second of raw data. The time between collisions will be 25 ns, however, due to the electronic delay, the detector can only respond in 2.5 μs. To deal with this problem, there are three trigger levels: the levels L1, L2 and the Event Filter. The L2 and the Event Filter are part of the High Level Trigger (HLT).

The L1 trigger will select high p_T muons, electrons, photons, jets and τ leptons decaying in hadrons. The decision time of 2 μs includes the transmission of signals between the detector and the trigger electronics. After L1 has accepted an event, the data is read out, formatted and stored in readout buffers (ROBs), being available to L2 trigger and Event Filter. The L1 trigger also provides Regions of Interest (RoI). The RoIs are regions in η and ϕ where its selection process has identified interesting features in the event and also contains information of the criteria passed. After L1 trigger the rate will be reduced to about 75 kHz.

The electron/photon trigger algorithm, shown in Figure 3.6, indentifies 2×2 clusters of trigger towers in which at least one of the four possible two-tower sums (1×2 or 2×1) of the nearest-neighbour electromagnetic towers exceeds a pre-defined threshold. The isolation-veto thresholds are set for the 12-tower ring in the electromagnetic calorimeter, as well as for the 2×2 hadronic tower core sum behind the cluster and the 12-tower hadronic ring around it. All these thresholds are programmable. The τ algorithm uses the same basic elements to select narrow hadronic jets.

These algorithms are run over all possible 4×4 windows. This implies that an electron/photon or τ cluster can satisfy the algorithm in two or more neighbouring windows. Multiple-counting of clusters is avoided by requiring the sum of the four central electromagnetic plus the sum of the four hadronic towers to be a local maximum with respect to its eight nearest overlapping neighbours. The location of this 2×2 local maximum also defines the coordinates of the electron/photon or τ RoI.

The L2 trigger uses about 2% of total event data at full granularity and precision, and it will reduce the trigger rate to 3.5 kHz. At this stage, the

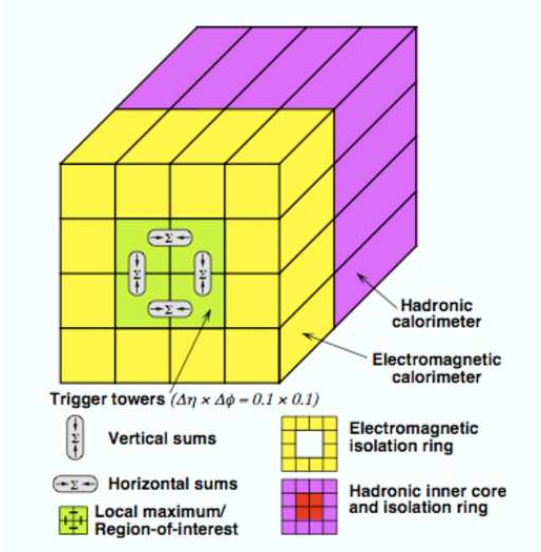

Figure 3.6: *Electron/photon and τ trigger algorithms.*

treatment time for an average event is 10 ms and at final stage, provided by the Event Filter, the rate will be reduced to 100 Hz.

The data acquisition system receives and buffers the event data at the L1 trigger accept rate moving the data within the RoIs to the L2 trigger. The events selected by the L2 trigger are moved to Event Filter and those that fulfill this last selection criteria are finally stored in the permanent event storage[18].

3.4 GRID

The LHC Computing Grid, is a distribution network designed to analyse 15 Petabytes (15 million Gigabytes) of data annually produced by the Large Hadron Collider (LHC) [19].

The data from the LHC experiments will be distributed around the globe, according to a four-tiered model. A primary backup will be recorded on tape at CERN, the Tier-0. The CERN computer center, considered "Tier 0" of the LHC Computing Grid, has a dedicated 10 Gb/s connection to the counting room. This data will be distributed to eleven large computer centres with

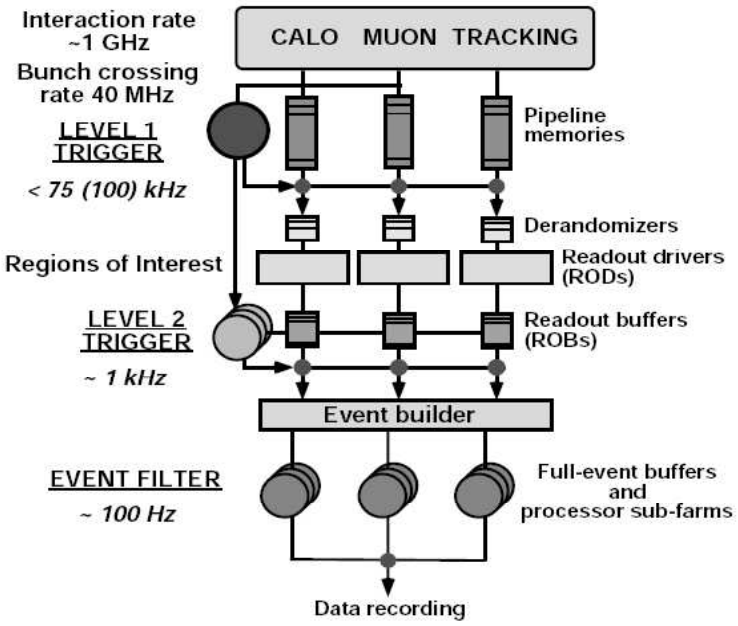

Figure 3.7: *ATLAS trigger scheme.*

sufficient storage capacity, the Tier-1 centres in Europe, Asia, and North America, via dedicated 10 Gb/s links. The Tier-1 centres will make data available to more than 150 Tier-2 centres, each consisting of one or several collaborating computing facilities, which can store sufficient data and provide adequate computing power for specific analysis tasks. Individual scientists will access these facilities through Tier-3 computing resources, which consist of local clusters.

Chapter 4

Generation and Simulation of Events

The generators used for all relevant processes in this study are presented in this chapter. The fast simulation libraries ATLFAST and ATLFASTb are also introduced.

4.1 Generation of events

All single top and $t\bar{t}$ processes were generated using the TopReX 4.10 library [20]. The TopReX is an event generator of top quark and Higgs boson production processes from pp and $p\bar{p}$ colisions, and generates high energy processes as well as the decay of the resulting particles. All these events were generated assuming the top mass $m_t = 175\,\text{GeV}$ and the W boson mass $m_W = 80.41\,\text{GeV}$

The background channels without top quarks ($b\bar{b}$, $W + jets$, $Z + jets$, WW, ZZ and WZ) were generated using the PYTHIA 6.228 library [21]. Since color charged particles cannot be isolated singularly due to confinement, and therefore cannot be directly observed, jets of many color-neutral particles clustered together are created and detected. The events were hadronized with PYTHIA and only CTEQ6L Parton Distribution Functions [22] were used in the simulation. The number of generated events is shown on Table 4.1.

The Parton Distribution Functions are probability distributions of the

longitudinal momentum fraction x of quarks and gluons inside a proton at momentum transfer Q^2. Since Parton Distribution Functions provide the partonic structure of hadrons, they allow the calculation of production cross sections at hadron colliders. Because of the inherent non-perturbative effect in a QCD binding state, parton distribution functions cannot be obtained by perturbative QCD. Due to the limitations in present lattice QCD calculations, the known parton distribution functions are instead obtained by using experimental data. The scale of Q^2 was set at $\sqrt{m_t^2 + p_T^2(top)}$. An example of a parton distribution function is shown in Figure 4.1.

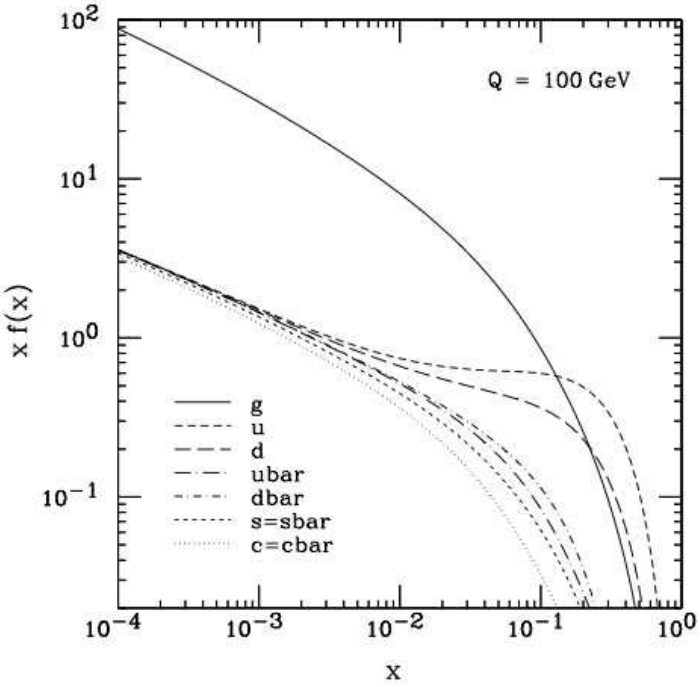

Figure 4.1: *CTEQ6M Parton distribution function for $Q = 100$ GeV. The value of $f(x)dx$ is the number of quarks or gluons with momentum fraction between x and dx of the proton momentum.*

In order to study the systematic uncertainties, several parameters were changed at the generation level. For instance, the analysis was done taking in consideration the Initial State Radiation and Final State Radiation (ISR and FSR). However, some samples were generated without ISR/FSR in order

Process	Generator	Number of events	Lum. (fb^{-1})
singletop (t-channel)	TopReX	2.7×10^7	109.49
singletop (s-channel)	TopReX	1×10^7	155.76
singletop Wt production	TopReX	1×10^7	938.37
$t\bar{t}$ semileptonic without taus	TopReX	4×10^7	48.02
$t\bar{t}$ semileptonic with taus	TopReX	4×10^7	48.02
$t\bar{t}$ hadronic	TopReX	4×10^7	48.02
$t\bar{t}$ dileptonic	TopReX	4×10^7	48.02
$W + jets$	Pythia	1.05×10^8	1.25
$Z + jets$	Pythia	7.5×10^7	2.31
$b\bar{b}$	Pythia	1.5×10^8	0.0050
WZ, WW, ZZ Pairs	Pythia	1.75×10^7	47.27

Table 4.1: *Number of generated events for each process and respective luminosity.*

to evaluate the associated error. Furthermore, in order to evaluate the effect of the top mass uncertainty, new single top samples for different top masses were generated with TopReX 4.10.

To study the overlap of events caused by independent hadron-hadron interactions, also known as pile-up, new samples were generated to include this processes and make the evaluation of the effect possible. Finally, the Peterson/SLAC function was used for the fragmentation of the bottom quark.

4.2 Simulation of events

The ATLFAST and ATLFASTb [23] are fast simulation libraries of the ATLAS detector. These programs simulate the deposition of energy of all stable particles of each event in the calorimeters cells, providing a list of reconstructed jets, leptons and missing transverse energy. The calorimeters cells are grouped inside a $\Delta R = 0.4$ cone region and only groups with transverse energy larger than 5 GeV are considered.

For electrons, the variation of momentum is done using a gaussian parameterization while, for muons, it depends on the transverse momentum, η and ϕ. The electrons momenta resolution in energy is $\sigma_E/E < 2.9\%$ for

an energy $E > 10\,\text{GeV}$ and for muons with $p_T < 100$ GeV, the resolution is $\sigma_{p_T}/p_T \leq 2\%$. These leptons are only selected if $|\eta| < 2.5$, $p_T > 5$ GeV for electrons and $p_T > 6$ GeV for muons. The leptons are classified as isolated if the transverse energy inside the cone $\Delta R = 0.2$ does not exceed the particle energy in 10 GeV. The energy depositions, which are not linked to isolated photons, muons or electrons, are used in the jet reconstruction.

The momentum variation of the jets is done with a $|\eta|$ dependent gaussian distribution. The jets are selected if $E_T > 10$ GeV and for this values, the resolution in energy is better than 12% if $|\eta| < 3$ and better than 24% if $|\eta| > 3$.

In the ATLAS detector, the b jets are possible to identify for $|\eta| < 2.5$. The b-tagging algorithm was simulated setting the efficiency at 60%, with 14.9% and 1.1% contamination for c jets and light jets, respectively.

Due to hadronization and FSR, the jets are reconstructed with lower energy than the original quarks and gluons. The ATLFASTb program is used to calibrate the energy of the jets using the calibration factor $K^{jet} = p_T^{partons}/p_T^{jet}$, which is the ratio between the energy of the parton and the reconstructed energy, obtained from reference samples. This factor depends on p_T and takes different values for b jets and light jets.

Chapter 5

Events Selection

In this chapter it is presented an event selection analysis at a luminosity of 10 fb^{-1} for the leptonic t-channel single top quark production under the structure of the LipCbrAnalysis program [24, 25]. The event selection analysis is divided in two different analysis, a sequencial analysis and a probabilistic one. Both analysis were developed in order to eliminate most of the background contamination, maximizing the ratio signal/background and also the signal significance.

5.1 Single top t-channel

In this analysis the signal is the single top t-channel. The W resulting from the Wtb vertex, may decay leptonically or hadronically, however, only the decay in electrons or muons was included in the signal. Therefore, the list of background channels includes $b\bar{b}$, W+jets, Z+jets, WZ pairs, $t\bar{t}$ and the rest of single top channels. The leptonic single top t-channel topology at the final stage is composed by a lepton (electron or muon), a b-jet, a non b-jet and missing energy due to the neutrino as shown in Figure 5.1. At the generation level, only events with at least one lepton with p_T above 20 GeV were created for signal and background. The event selection was divided in two levels, a sequencial analysis comprising several kinematical and geometrical cuts on the reconstructed objects and a discriminant analysis based on the probability of a given event to be signal or background like.

The detector only provides information about final particles for each event. For the signal events, the detector is expected to efficiently reconstruct a non-b jet, to tag a b-jet with an efficiency of 60% and identify an electron or muon within the fiducial volume. The neutrino is not directly detected but can be reconstructed from the missing transverse momentum. For the signal, the W boson decays into an electron or a muon which implies:

$$p^{\mu}p_{\mu} = m_W^2 = m_l^2 + 2E_lE_{\nu} + 2\vec{p}_l.\vec{p}_{\nu} \approx 2E_lE_{\nu} + 2\vec{p}_l.\vec{p}_{\nu} \tag{5.1}$$

Assuming the W boson on-shell, with $m_W = 80.4\,\mathrm{GeV}$, and stating that the neutrino transverse momentum matches the missing transverse momentum, it is possible to determine the z momentum component of the neutrino. However, if a solution exists, there are two possible solutions. In this analysis, the chosen neutrino solution is the one with lower momentum along the z-axis, this solution holds a purity of about 60%. With the neutrino fully reconstructed it is possible to reconstruct the W boson and the top quark.

5.2 Pre-selection

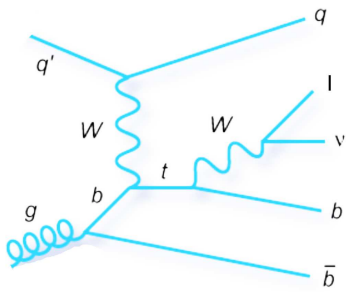

Figure 5.1: *Leptonic single top t-channel.*

At the preselection level, several cuts are made in order to reject most of background events and keep a large fraction of the signal. These cuts match the topology of the single top t-channel and are presented in the list below:

- 1 lepton ($P_{\mathrm{T}} > 25\mathrm{GeV}; |\eta| < 2.5$)

- Missing $E_{\mathrm{T}} > 20\mathrm{GeV}$
- $m_{\mathrm{T}}^{W} > 25\mathrm{GeV}$; $15 < P_{\mathrm{T}}^{W} < 215\mathrm{GeV}$
- 1 b-jet ($P_{\mathrm{T}} > 50\mathrm{GeV}$;$|\eta| < 2.5$)
- 1 non b-jet ($P_{\mathrm{T}} > 40\mathrm{GeV}$)
- $H_{\mathrm{T}} > 180\mathrm{GeV}$
- $100 < m_{\mathrm{T}} < 500\mathrm{GeV}$

Some relevant normalized distributions are shown in Figure 5.2 before the pre-selection cuts. The determination of each cut was based on the behaviour of the respective distributions, in order to increase the signal/background ratio and the signal significance. For instance, the choice of one lepton is clearly the best option to proceed into a cleaner analysis. Furthermore, a set of kinematic variables such as the missing transverse momentum, the W transverse mass, the W transverse momentum, the b-jet transverve momentum, the non-b jet transerve momentum and H_{T} (sum of transverse momentum of all objects and the missing transverse momentum) turn out to be very useful to isolate the signal.

The number of events for signal and background channels after the pre-selection cuts are presented on table 5.1. The dominant backgrounds at this level are the W+jets and $t\bar{t}$ channels. Since the pre-selection can only provide a signal/background ratio lower than 0.5 and it is not able to eliminate these backgrounds, a likelihood-based analysis was developed to accomplish this goal. The same normalized distributions shown in Figure 5.2 are presented after the pre-selection cuts in Figure 5.3.

5.3 Discriminant analysis

After the pre-selection, six different signal and background probability density functions (p.d.f.) were created from a set of relevant kinematical variables.

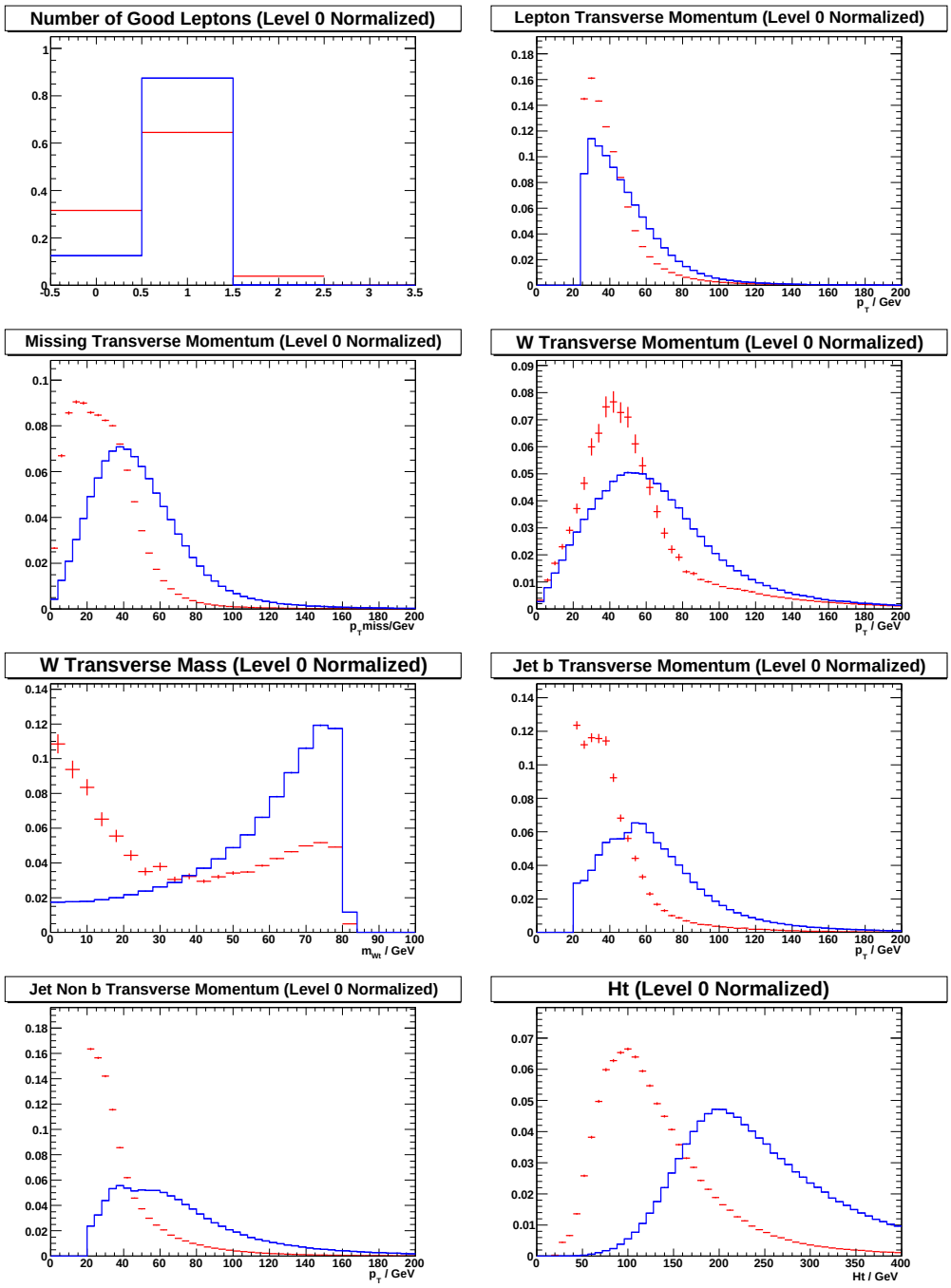

Figure 5.2: *Distributions before the pre-selection for signal and background (the signal is in blue and the background is in red).*

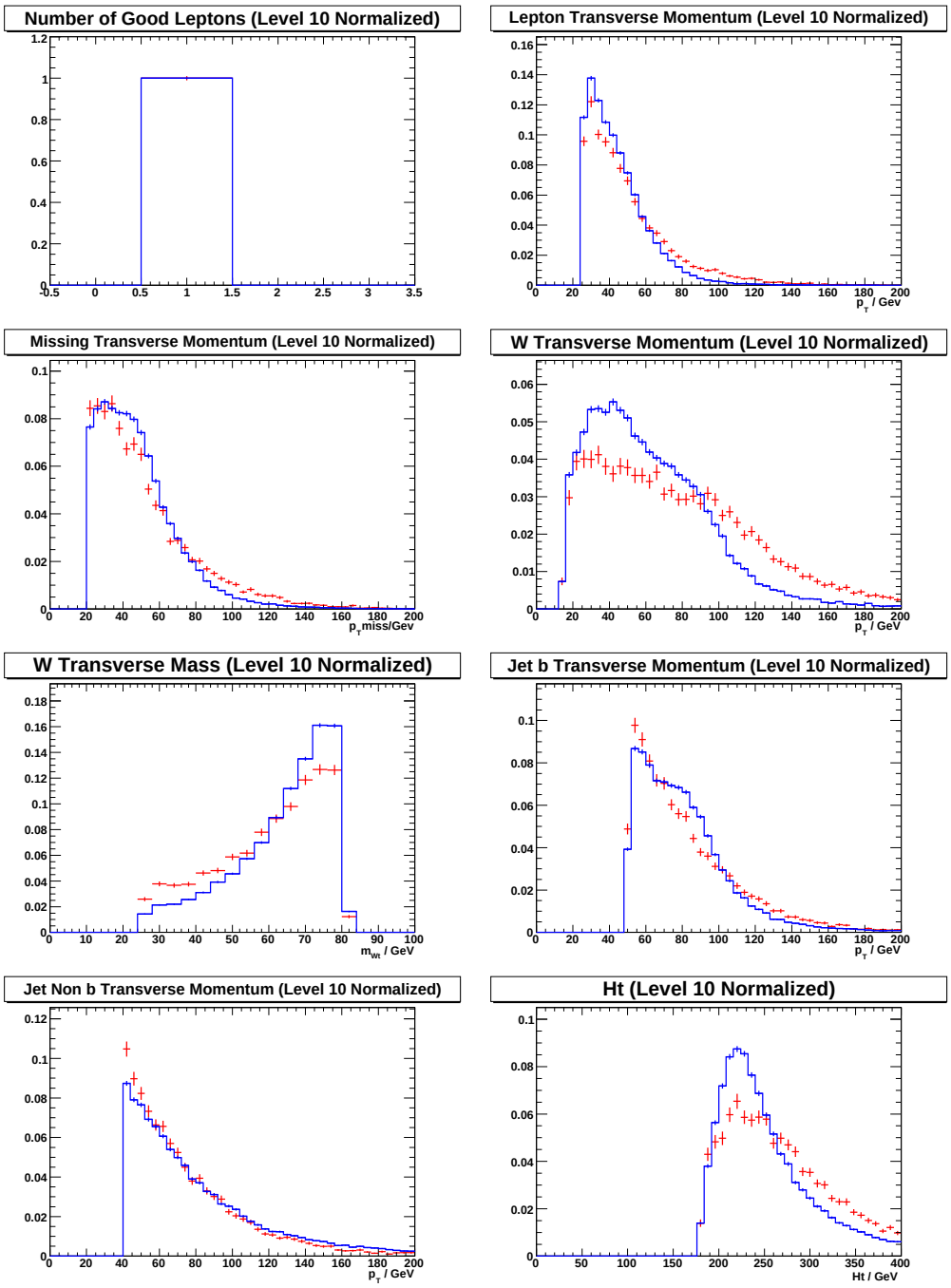

Figure 5.3: *Normalized distributions after the pre-selection for signal and background (the signal is in blue and the background is in red).*

Process 10 fb^{-1}	Pre-Selection
Signal (t-channel, $l = e, \mu$)	17007±68
Z+jets	1290±75
W+jets	20501±404
WZ pairs	195±5
single top (other)	3816±19
$t\bar{t}$	13401±53
total SM bkg.	39203±415

Table 5.1: *Number of events after the pre-selection level normalized to 10* fb^{-1}.

For a given event, the probability to be signal $\mathcal{P}_i^{signal}$ or background $\mathcal{P}_i^{background}$ is calculated from each probability density function. A new variable, named signal likelihood, is defined as the product of the probabilities of the event to be signal, $\mathcal{L}_S = \prod_{i=1}^{n} \mathcal{P}_i^{signal}$ with n = number of p.d.f. Through the same process, the background likelihood is defined as $\mathcal{L}_B = \prod_{i=1}^{n} \mathcal{P}_i^{background}$. With these two new variables, the discriminant variable, likelihood, is defined as:

$$L_R = \ln \frac{\mathcal{L}_S}{\mathcal{L}_B} \tag{5.2}$$

The variables chosen for the probability density functions must have different behaviours for signal and background, providing an efficient discrimination between them. The list of the probability density functions, shown in Figure 5.5 after the pre-selection cuts, used in this analysis is:

- Cosine of the angle between the lepton and the non-b jet in the Top quark rest frame.
- W boson transverse momentum.
- Top quark mass.
- η of the non-b jet.
- Cosine of the angle between the b-jet in Top quark rest frame and the Top quark in the Top/non-b jet rest frame.

- η of the top quark.

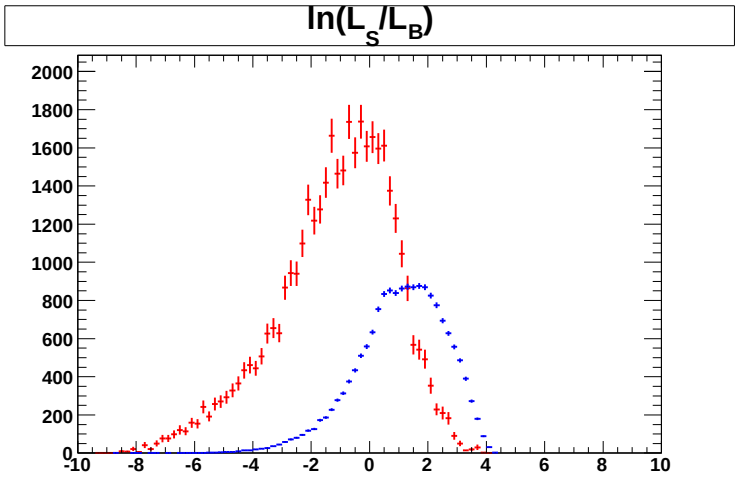

Figure 5.4: *Likelihood variable for signal (blue) and background (red).*

The likelihood distribution built with these p.d.f.s is shown in Figure 5.4. The last level of the event selection is the cut on the likelihood variable at $L_R > 1.75$, maximizing the signal/background ratio to about 3.5. The number of events selected is presented on table 5.2 and shows the efficiency of the discriminant analysis on the rejection of the dominant backgrounds, $t\bar{t}$ and W+jets.

Process 10 fb^{-1}	Final Selection
Signal (t-channel, $l = e, \mu$)	6005±41
Z+jets	130±24
W+jets	1069±92
WZ pairs	3±1
ST	275±7
$t\bar{t}$	348±9
total SM bkg.	1826±96

Table 5.2: *Events at final selection level normalized to 10* fb^{-1}.

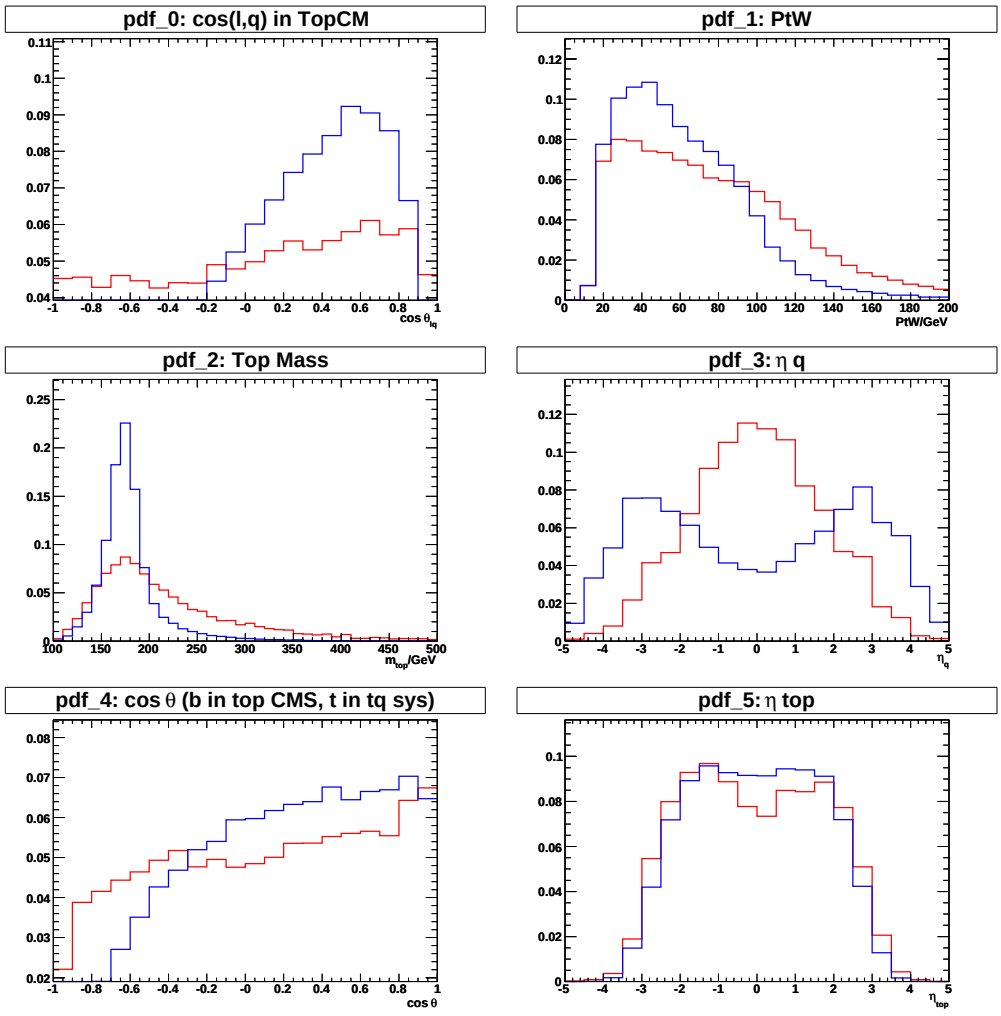

Figure 5.5: *Probability density functions for signal (blue) and background (red).*

Chapter 6

Results

In this chapter, the results for the angular and spin asymmetries are presented as well as the respective statistical and systematic uncertainties. From these results, the limits on anomalous couplings were calculated using the TopFit library [4, 5].

6.1 Angular asymmetries

The simulated angular distribution $\cos\theta_l^\star$, from which the angular asymmetries are determined, includes the signal and all the Standard Model backgrounds. This distribution is affected by the experimental resolution, reconstruction and selection criteria. After subtracting the reference background sample to the fake data sample, the distribution must be multiplied by the correction function in order to recover the Standard Model distribution. The correction function is calculated, for each bin of the corresponding distribution, dividing the number of events at the generator level by the number of events after the event selection, using a reference sample. In summary, there are two equivalent signal samples, S_1 and S_2, two equivalent background samples, B_1 and B_2, and a generator sample corresponding to the Standard Model:

- Fake data sample: $D = S_1 + B_1$;
- Signal reference sample: S_2;

- Background reference sample: B_2;
- Correction function: $f_c = \frac{G}{S_2}$;
- Corrected distribution: $(S_1 + B_1 - B_2) \times \frac{G}{S_2}$;

The corrected distribution, the standard model distribution and the correction function obtained for the angular variable $\cos\theta_l^\star$ are shown in Figure 6.1.

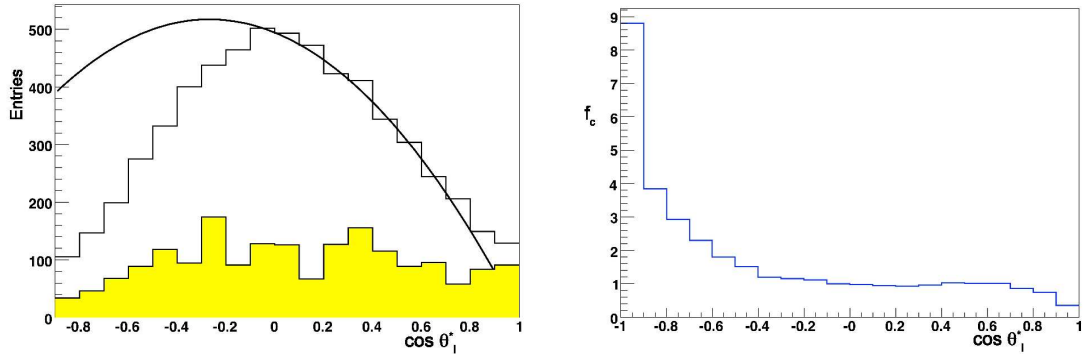

a) b)

Figure 6.1: *a) Simulated* $\cos\theta_l^\star$ *distribution. b) Correction Function. In the first plot, the signal (full histogram) and the SM background (shaded histogram) are normalized to* $L = 10\,fb^{-1}$*. The SM distribution is also shown (full curve).*

The results obtained for the angular asymmetries after correction, and the respective statistic uncertainties, are:

$$A_{FB} = -0.1937 \pm 0.0240$$
$$A_+ = 0.5883 \pm 0.0301$$
$$A_- = -0.8385 \pm 0.0123$$

Due to the large statistics available at LHC, the systematic errors play an important role in the measurent of angular distributions and asymmetries. The systematic errors in the studied observables are estimated by calculating them with various reference samples and observing the differences obtained. The uncertainties are considered to come from the following sources [26]:

- Structure functions: The correction function obtained from a reference sample generated with CTEQ6L PDFs is applied to samples generated with MRST2001 PDFs in order to estimate the effects on the correction function, and thus on the observables. The deviations found are considered as the systematic error associated to the structure functions.

- Top quark mass dependence: Samples corresponding to top quark masses of 170, 175 and 180 GeV are simulated, and the influence of m_t on the values obtained for the corrected observables (using correction functions for $m_t = 175$ GeV) is determined. The systematic error used here is obtained from a linear fit of the values found corresponding to a top mass uncertainty of 2 GeV.

- ISR and FSR: The effect is studied creating an event sample in which ISR and FSR are switched off in the event simulation. The results of the reference sample (with ISR and FSR) are compared with those obtained adding to it a normalised fraction of the sample without ISR nor FSR (from 0% to 25%, in steps of 5%). The values obtained for the observables are fitted with a linear function and the systematic error is considered as the effect of the presence of 20% (a conservative estimate of our level of knowledge of ISR and FSR) of the sample without ISR, FSR.

- b-jet tag efficiency: The value of the b-jet tag efficiency (and the corresponding c-jet and light-jet rejection factors) is varied from 50 to 70%, in steps of 10%, and the values obtained for the observables are fitted with a linear function. The systematic error is considered as the effect on the observables of a variation of 5% in the b-jet tagging efficiency, as compared with the standard value of 60%.

- b-jet energy scale: The value of the b-jet energy scale is changed from -7 to +7%, and the values obtained for the observables are fitted with a linear function. The systematic error is considered as the effect of a variation of 3% in the b-jet energy scale.

- Light-jet energy scale: The value of the energy scale of the light-jets is changed from -7 to +7%, and the values obtained for the observables

are fitted with a linear function. The systematic error is considered as the effect of a variation of 1% in the energy scale of the light jets.

- Background: The background (as obtained from the reference sample) subtracted to the selected sample is varied from -25 to 25%, in steps of 5%, and the values obtained for the observables are fitted with a linear function. The systematic error is considered as the effect of a variation of 10% on the background level (which takes into account the uncertainties in the cross-sections).

- Pile-up: The effect of pile-up events (2.3 events in average) is studied by comparing the values of the observables obtained with and without adding pile-up events.

- b-quark fragmentation: The parameter b in the Peterson parameterisation for b-quark fragmentation is changed from -0.006 to -0.0035, and the values obtained for the observables compared. The difference is considered as systematic error.

The sources of systematic errors in the evaluation of the angular asymmetries are summarized on Table 6.1 and the corresponding plots are shown in Figures 6.3, 6.5, 6.7, 6.9 and 6.11. These systematic uncertainties are larger than the statistic error for the three asymmetries and the dominant contributions are PDFs, Top Mass, Pile-up and b-quark fragmentation. The top mass systematic uncertainty value may be directly related to the narrow width of the top mass distribution, furthermore, the top quark mass was set at 175 GeV in the generation. However, it is expected that the LHC experiments provide an accurate measure of the top quark mass and therefore, reduce this uncertainty. The rest of the dominant contributions may be also reduced with an increase of statistics.

6.2 Spin asymmetries

The same procedure described on the previous section is now applied to the spin distributions, $\cos\theta_X$, shown in Figure 6.2. All these plots hold low

Source	A_{FB}	A_+	A_-
PDFs	0.0241	0.0028	0.0044
Top mass	0.0134	0.0158	0.0046
ISR+FSR	0.0000	0.0030	0.0046
b tag eff.	0.0004	0.0094	0.0063
Eb scale	0.0096	0.0035	0.0041
Ej scale	0.0004	0.0024	0.0001
Back.	0.0006	0.0031	0.0025
Pile-up	0.0156	0.0291	0.0018
b frag.	0.0133	0.0346	0.0081
Total syst.	0.0357	0.0493	0.0139

Table 6.1: *Systematic errors in the evaluation of the angular asymmetries.*

statistics on the last bins due to selection and detector cuts, therefore, it is expected that the corrected distributions show large fluctuations in these regions. The results for the spin asymmetries, their ratios and the respective statistical uncertainties are:

$$
\begin{aligned}
A_l &= 0.4280 \pm 0.0313 \\
A_\nu &= -0.1908 \pm 0.0251 \\
A_b &= -0.1462 \pm 0.0269 \\
r_{\nu l} &= \tfrac{A_\nu}{A_l} = -0.4458 \pm 0.0668 \\
r_{bl} &= \tfrac{A_b}{A_l} = -0.3416 \pm 0.0671
\end{aligned}
$$

The sources considered in the evaluation of the systematic uncertainties of the spin asymmetries and their ratios are the same as used for the angular asymmetries. These are summarized on Table 6.2 and the corresponding plots are shown in Figures 6.4, 6.6, 6.8, 6.10 and 6.12. Similarly to the angular asymmetries, the Pile-up, the b-quark fragmentation and the PDFs are dominant sources of systematic uncertainties which can be possibly reduced with an increase of statistics. However, the b-jet energy scale arises for these observables becoming the most important contribution.

Source	A_b	A_ν	A_l	$r_{\nu l}$	r_{bl}
PDFs	0.0114	0.0072	0.0102	0.0063	0.0356
Top mass	0.0013	0.0014	0.0034	0.0069	0.0058
ISR+FSR	0.0011	0.0018	0.0261	0.0207	0.0216
b tag eff.	0.0038	0.0034	0.0011	0.0088	0.0096
Eb scale	0.0234	0.0093	0.0139	0.0369	0.0442
Ej scale	0.0053	0.0014	0.0046	0.0082	0.0090
Back.	0.0017	0.0032	0.0003	0.0072	0.0038
Pile-up	0.0103	0.0096	0.0045	0.0275	0.0207
b frag.	0.0197	0.0143	0.0042	0.0287	0.0489
Total syst.	0.0349	0.0215	0.0324	0.0604	0.0820

Table 6.2: *Systematic errors in the evaluation of the spin asymmetries.*

6.3 Limits on anomalous couplings

With the results obtained in the previous section, and the parametric dependence of the observables on V_R, g_L and g_R implemented into the library TopFit, constraints on the latter can be set.

The 1 σ limit on a coupling $x = V_R$; g_L;g_R can be roughly derived by finding the values of x for which O deviates one σ from its central value. Nevertheless, due to the quadratic dependence of the observables on V_R and g_L near the SM point $V_R = g_L = 0$, this procedure leads to overcoverage of the obtained coincidence intervals, because their p.d.f. is not Gaussian even if the p.d.f. of the observable O is [4, 26].

In order to obtain the limits on an anomalous coupling x, given by the measurement of an observable O, the p.d.f. of x is determined numerically, using the acceptance-rejection method iteratively:

- A random value (with uniform probability) x_i, within a suitable interval, is generated;
- The probability of O (x_i), given by the p.d.f. of O is evaluated;
- An independent random number r_i (with uniform probability) is gen-

erated;

- The value x_i is accepted if the probability of $O(x_i)$ is larger than r_i.

The resulting set of values $\{x_i\}$ is distributed according to the p.d.f. of x given by the measurement of O. The determination of a central interval with a given CL is done numerically, requiring [26]:

- that it contains a fraction of the total number of values $\{x_i\}$;
- that is central, i.e. fractions $(1-\gamma)/2$ of the values generated on each side of the interval;

The 1 σ limits are determined for each observable assuming only one coupling different from zero at each time. However, the limits may be improved combining measurements on different observables. The ATLAS expected 68% CL regions on the anomalous couplings in the Wtb vertex at the decay for $L = 10\,\text{fb}^{-1}$ were done using TopFit [4, 5] and are shown in Figure 6.13. The boundary of the regions were chosen as a contour of constant χ^2.

From the plots shown in Figure 6.13, one concludes that the combination of different observables, such as angular asymmetries and spin asymmetries ratios, is very useful to improve the limits. In particular, r_{bl} plays an import role due to its different dependence on the anomalous couplings of the Wtb vertex in comparison to other observables.

Furthermore, the limits on a given pair of anomalous couplings are also improved by setting the others at the SM value. It is also expected that a decrease in the systematic uncertainty contribution will improve the limits on the anomalous couplings so that they may be combined with those in $t\bar{t}$ channel.

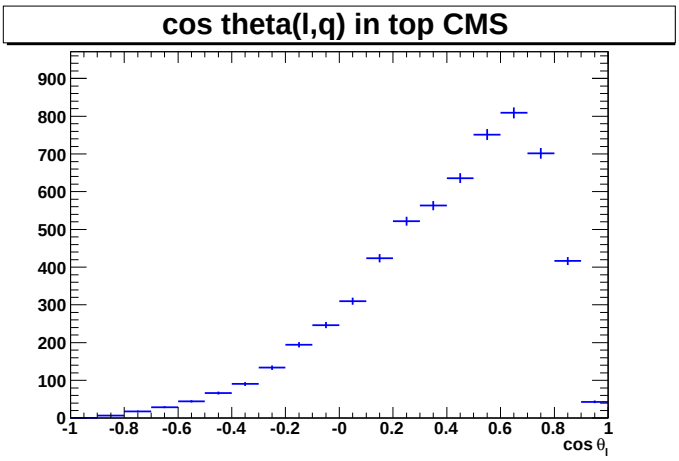

a)

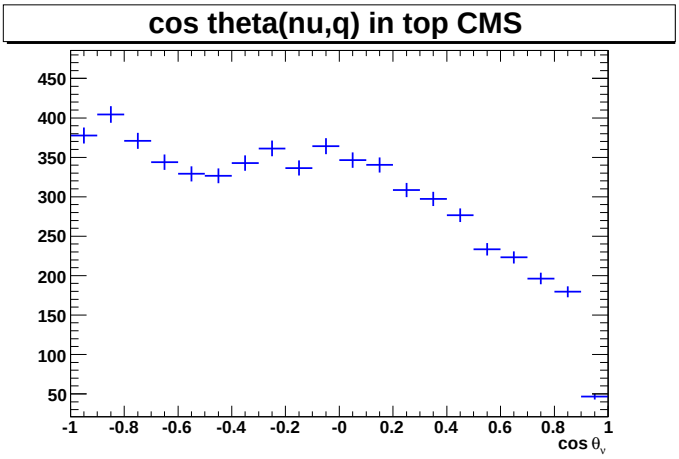

b)

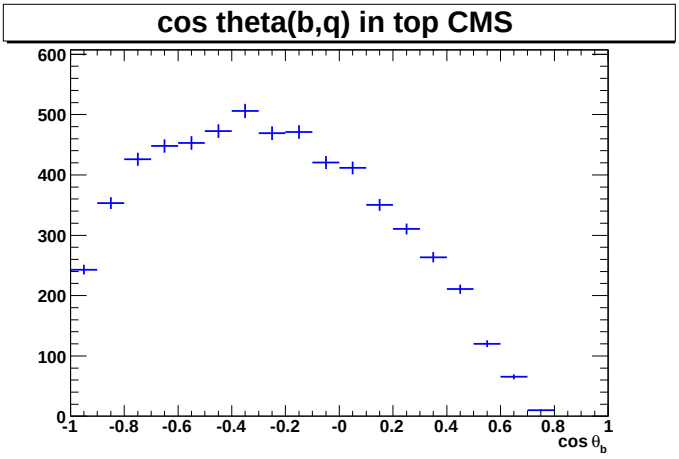

c)

Figure 6.2: *Signal* $\cos\theta_X$ *distribution after final selection: a)* X *= lepton, b)* X *= neutrino, c)* X *= b-jet*

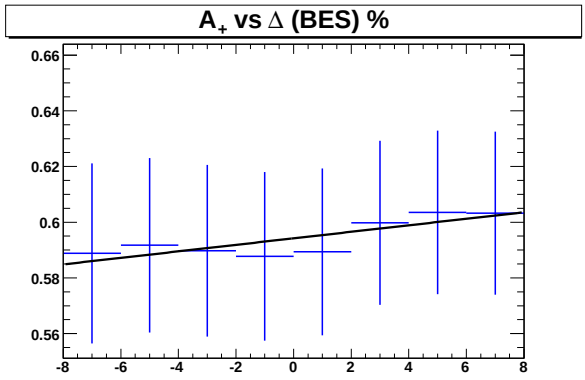

a)

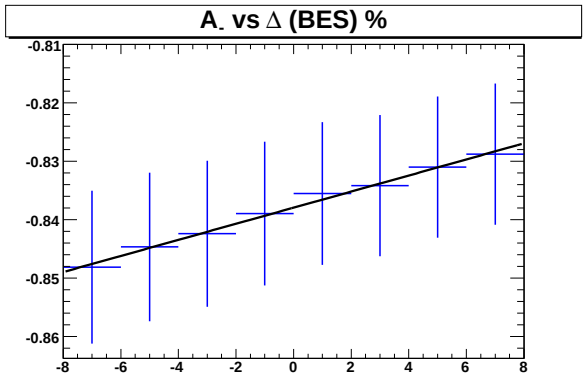

b)

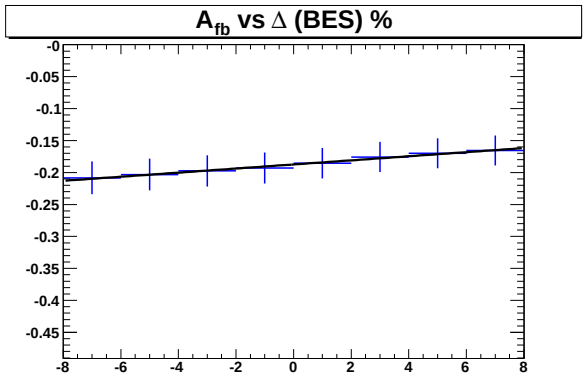

c)

Figure 6.3: *The dependence with the b-jet energy scale is shown, together with a linear fit, for a) A_+, b) A_-, c) A_{FB}*

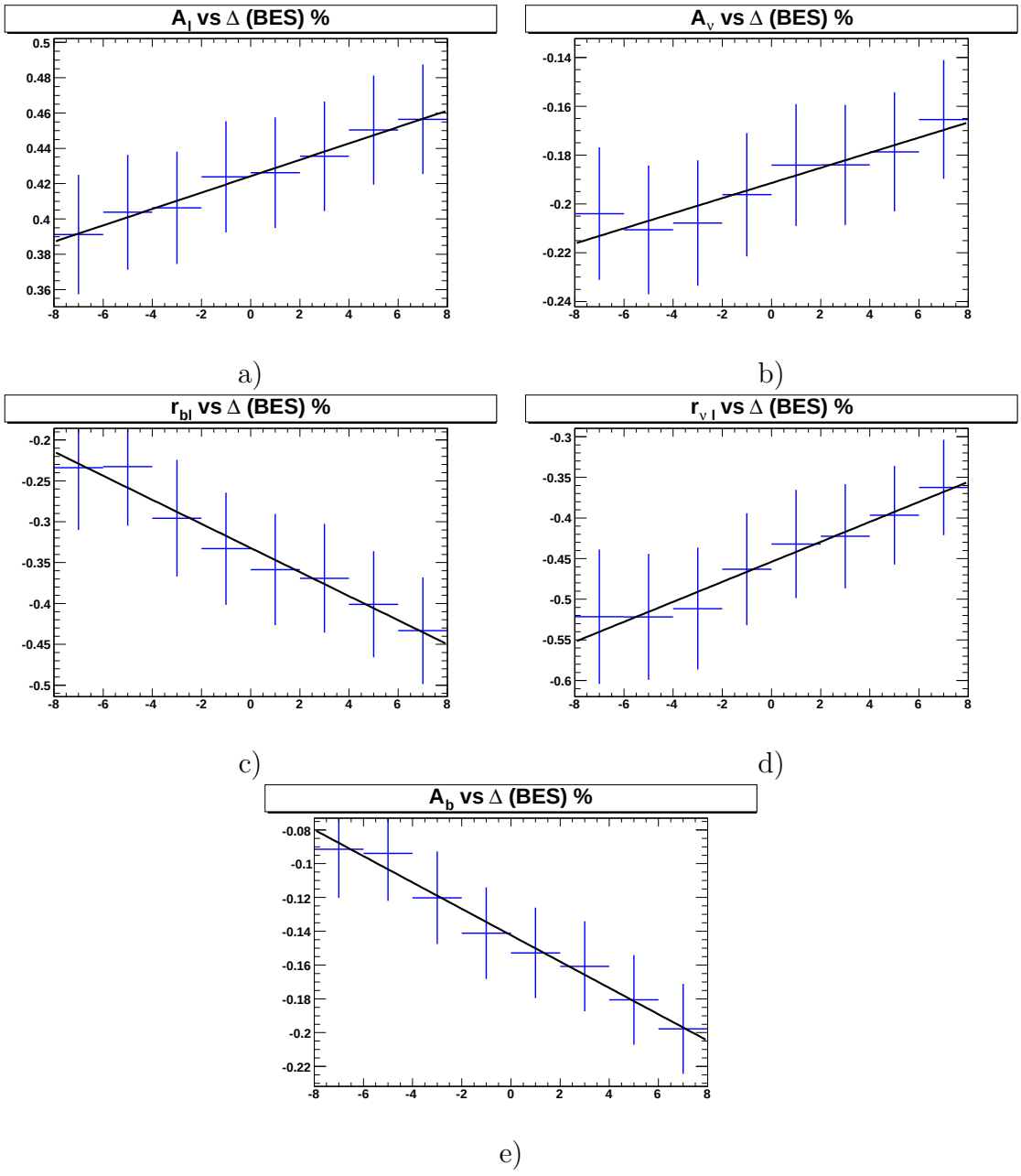

Figure 6.4: *The dependence with the b-jet energy scale is shown, together with a linear fit, for a) A_l, b) A_ν, c) r_{bl}, d) $r_{\nu l}$, e) A_b*

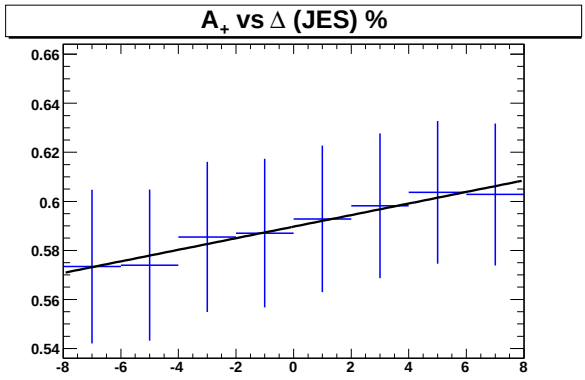

a)

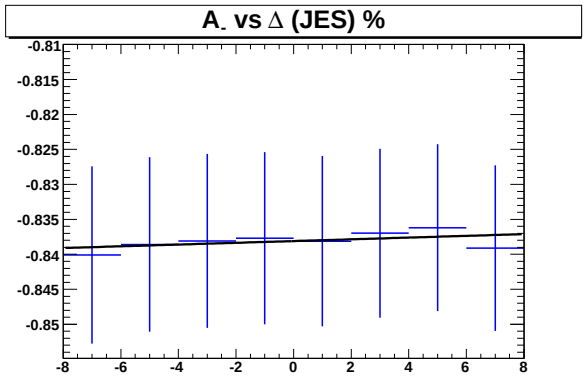

b)

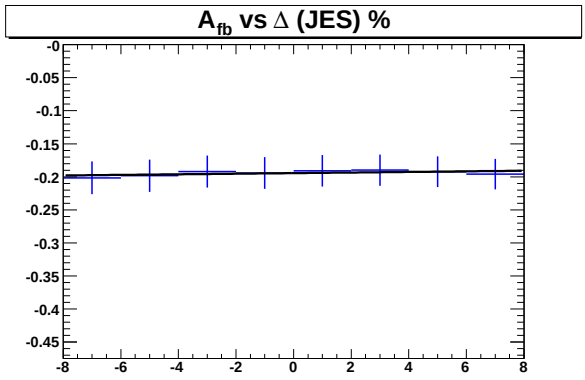

c)

Figure 6.5: *The dependence with the light jet energy scale is shown, together with a linear fit, for a) A_+, b) A_-, c) A_{FB}*

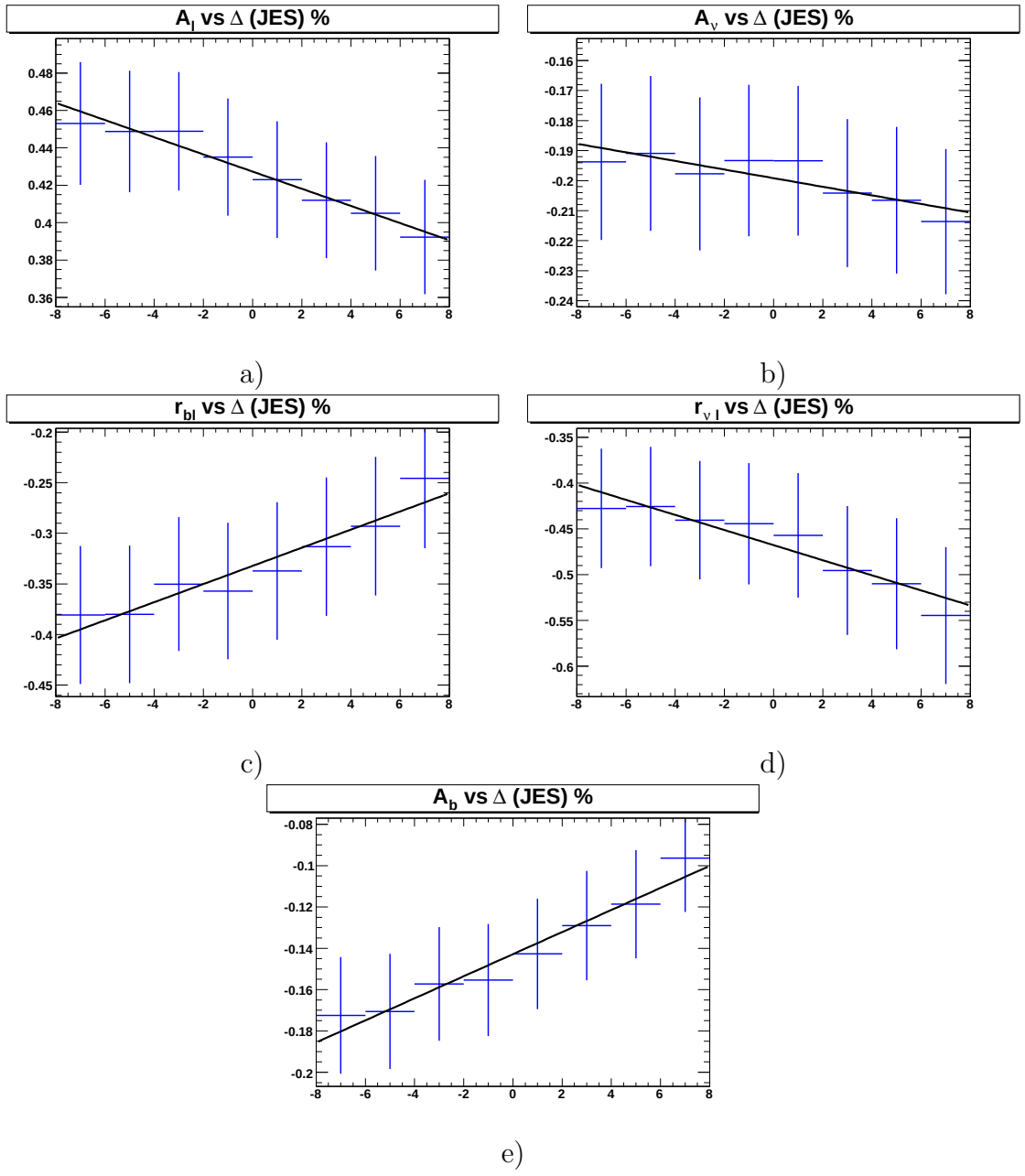

Figure 6.6: *The dependence with the light jet energy scale is shown, together with a linear fit, for a) A_l, b) A_ν, c) r_{bl}, d) $r_{\nu l}$, e) A_b*

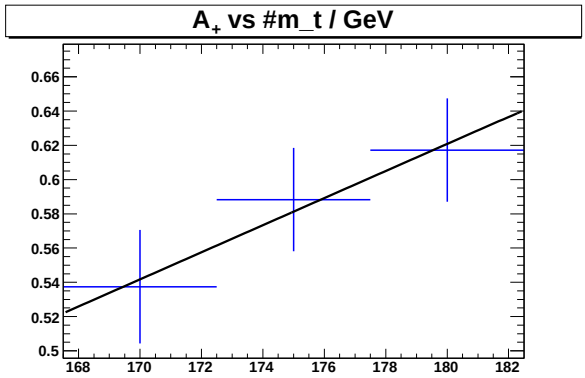

a)

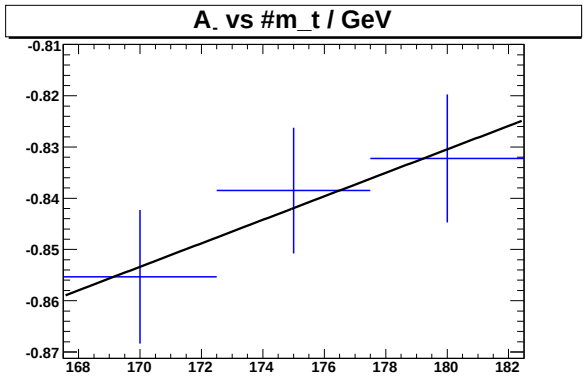

b)

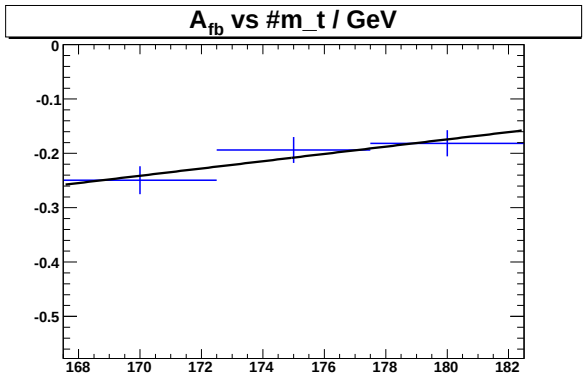

c)

Figure 6.7: *The dependence with the top mass is shown, together with a linear fit, for a) A_+, b) A_-, c) A_{FB}*

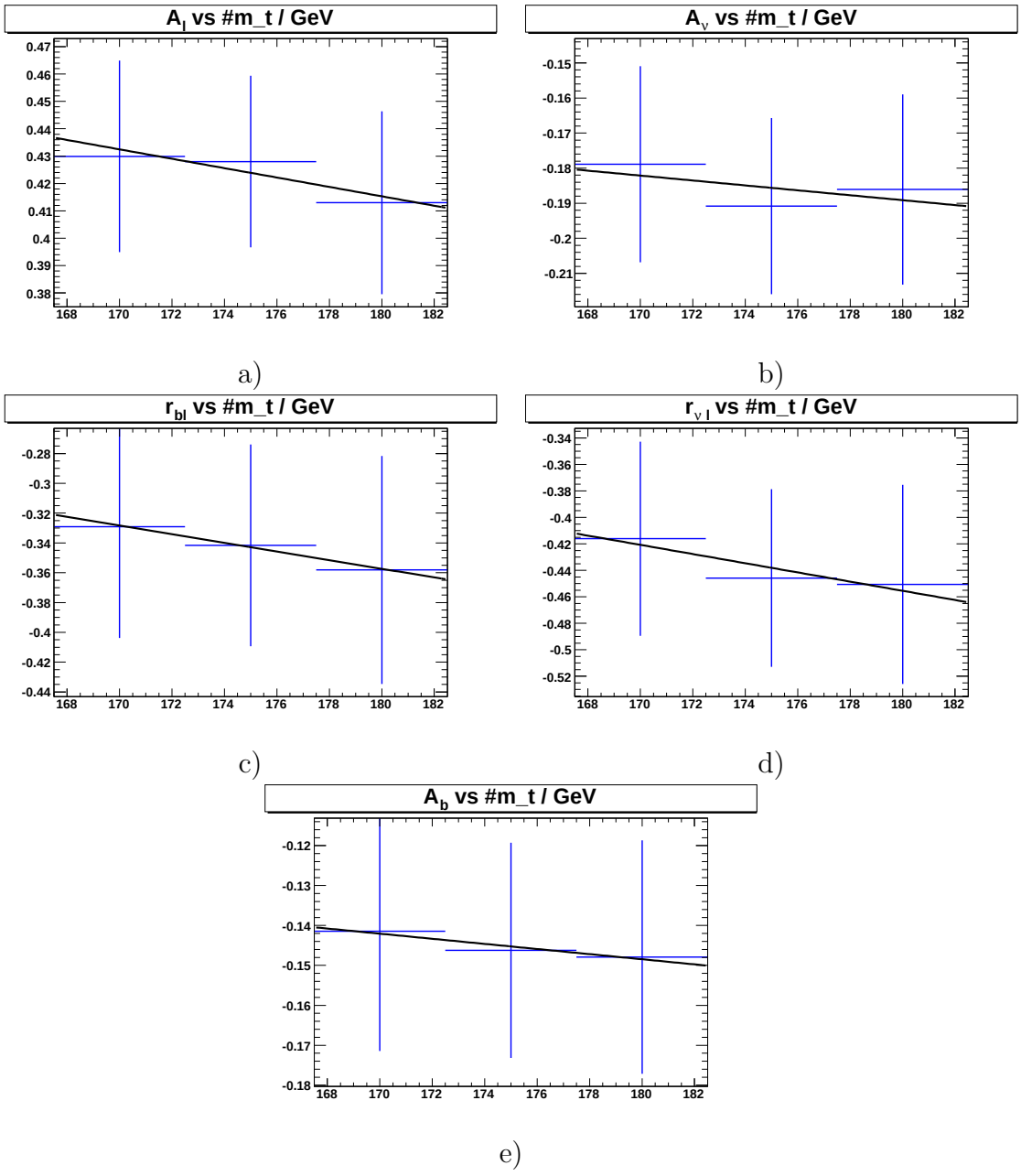

Figure 6.8: *The dependence with the top mass is shown, together with a linear fit, for a) A_l, b) A_ν, c) r_{bl}, d) $r_{\nu l}$, e) A_b*

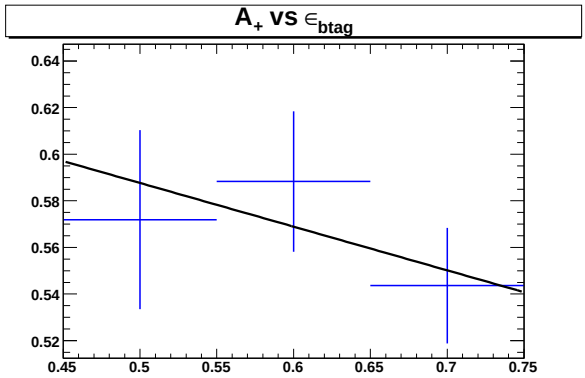

a)

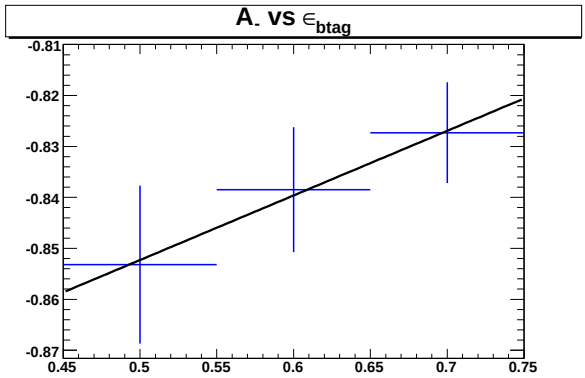

b)

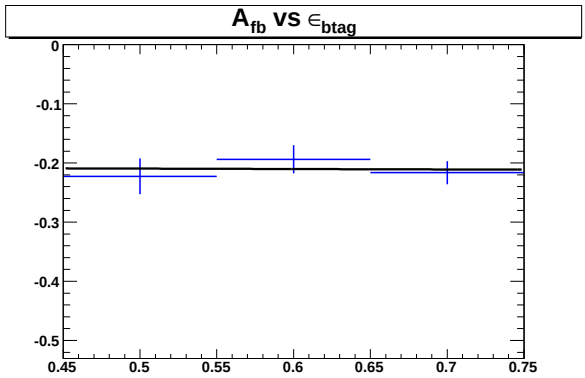

c)

Figure 6.9: *The dependence with the b-tag efficiency is shown, together with a linear fit, for a) A_+, b) A_-, c) A_{FB}*

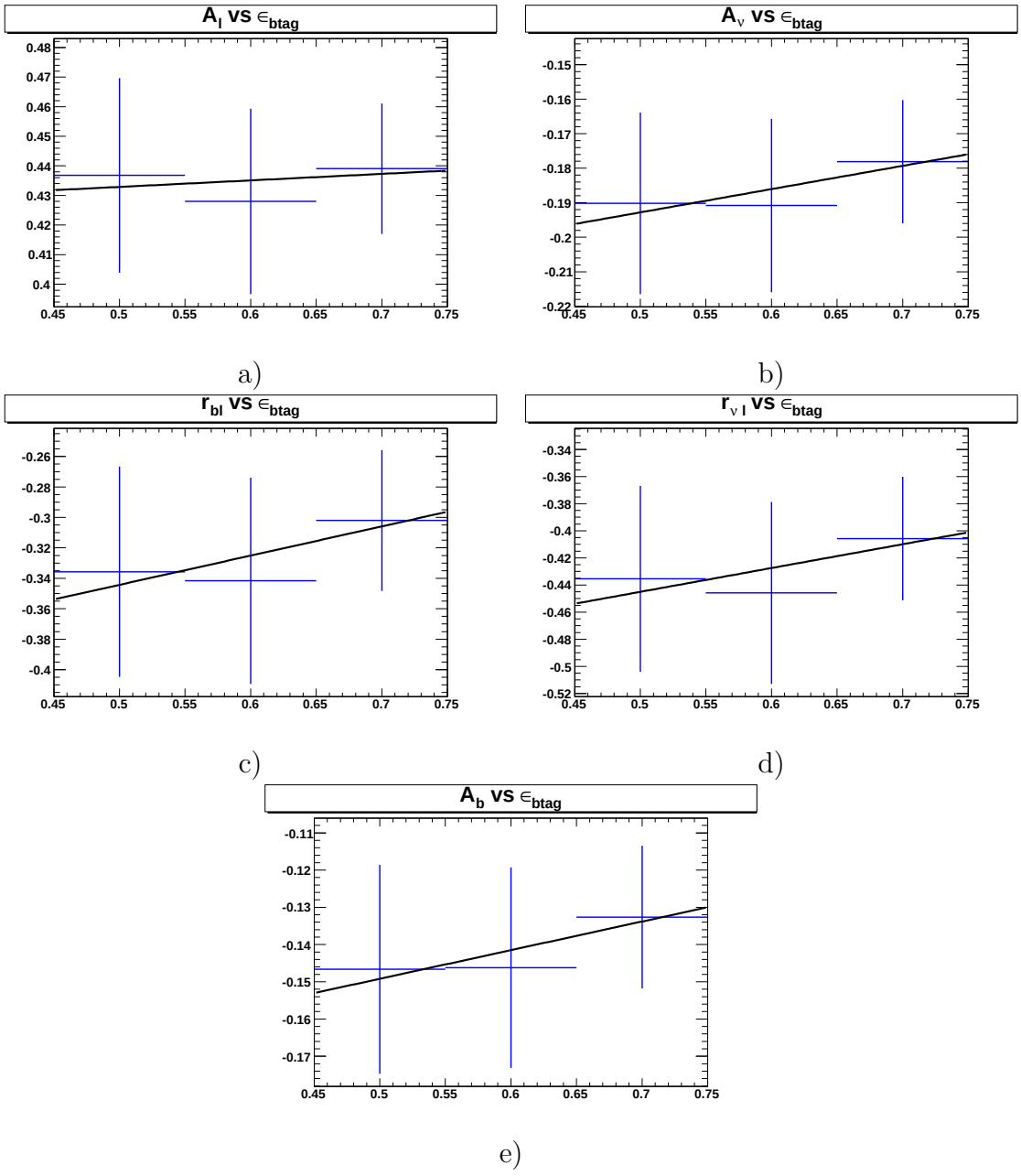

Figure 6.10: *The dependence with the b-tag efficiency is shown, together with a linear fit, for a) A_l, b) A_ν, c) r_{bl}, d) $r_{\nu l}$, e) A_b*

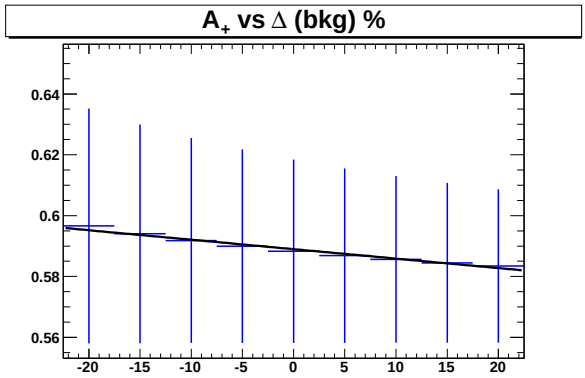

a)

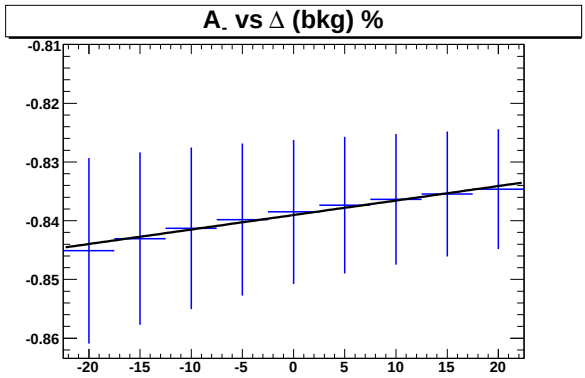

b)

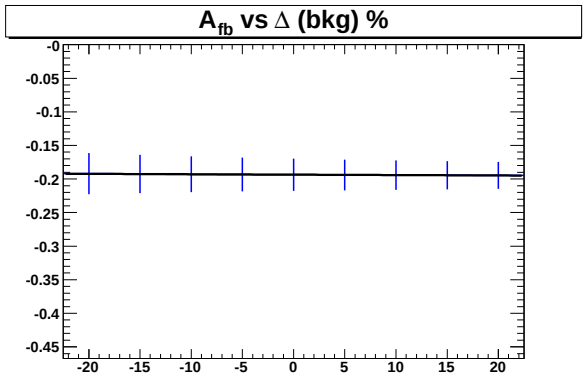

c)

Figure 6.11: *The dependence with the SM background uncertainty is shown, together with a linear fit, for a) A_+, b) A_-, c) A_{FB}*

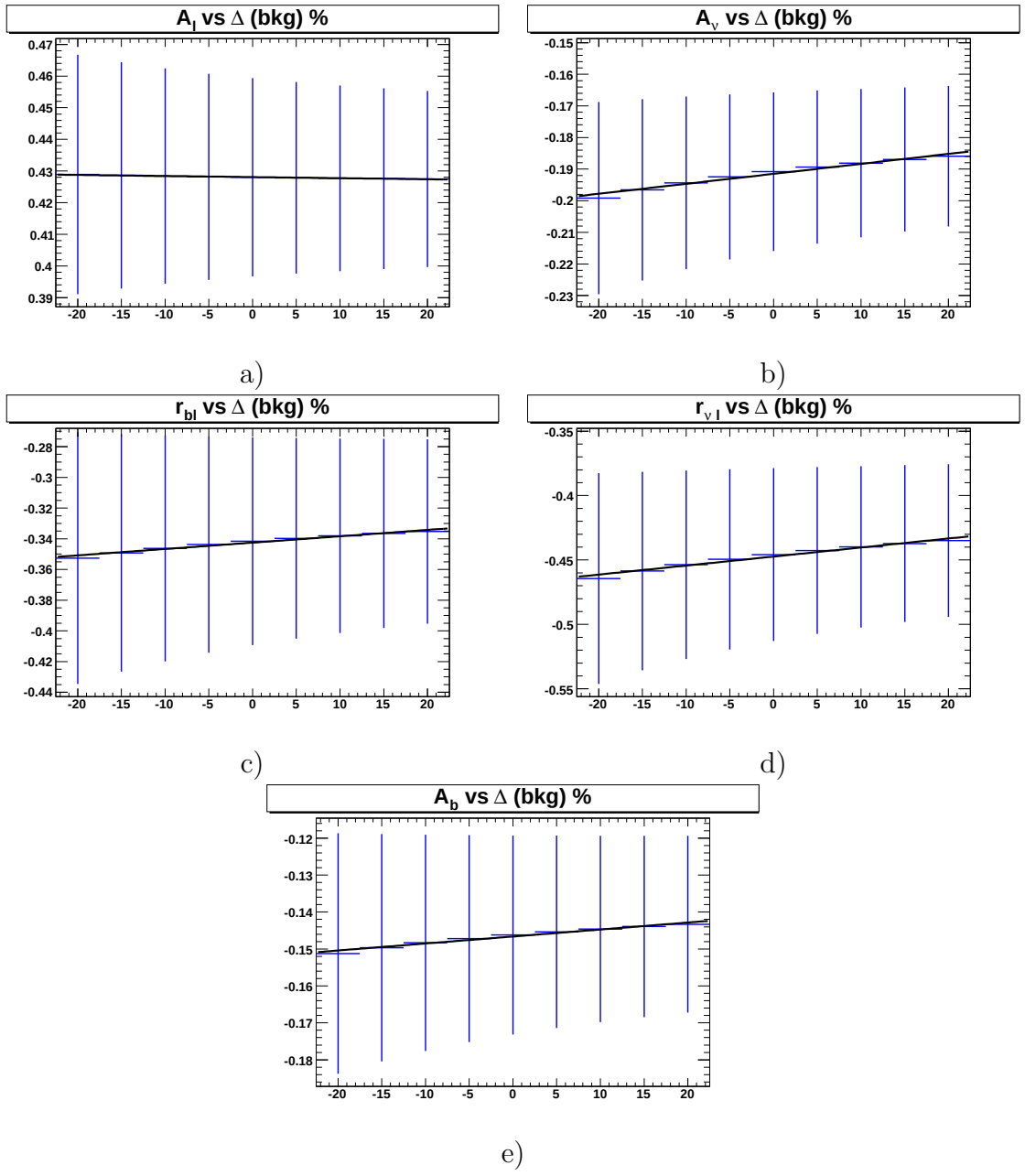

Figure 6.12: *The dependence with the SM background uncertainty is shown, together with a linear fit, for a) A_l, b) A_ν, c) r_{bl}, d) $r_{\nu l}$, e) A_b*

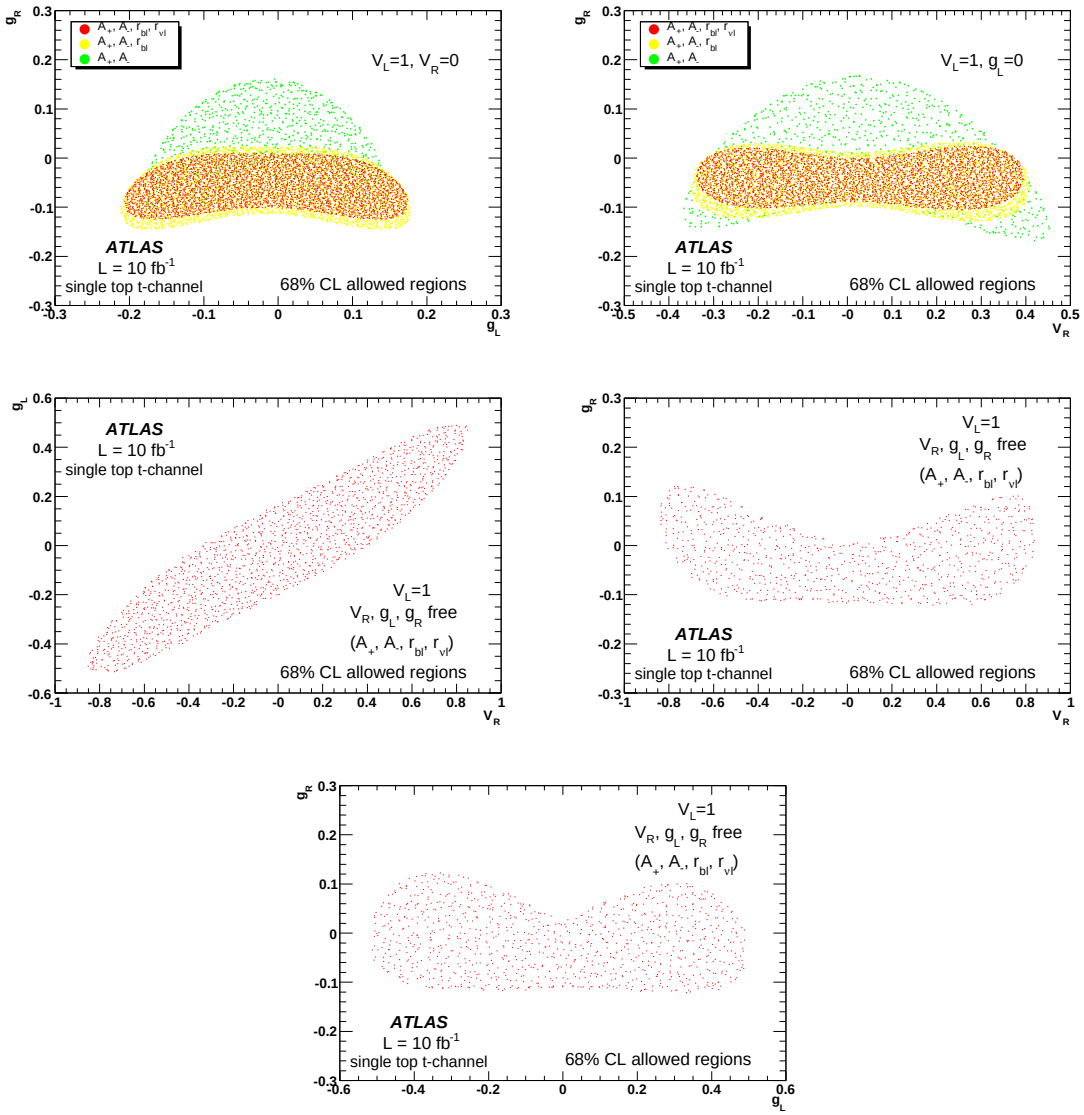

Figure 6.13: *ATLAS expected 68% CL regions on the anomalous couplings at* $L = 10\,\mathrm{fb}^{-1}$ *for different observables and anomalous couplings combinations.*

Chapter 7

Conclusions

In this work, the ATLAS sensitivity to the leptonic t-channel single top quark production was studied. A sequential analysis and a discriminant one were developed to select the signal events and eliminate the background. The discriminant analysis after the sequential one became very useful to eliminate the $t\bar{t}$ and $W + jets$ background channels, providing an important increase to the signal/background ratio. Furthermore, after applying correction functions to correct the effects of the experimental resolution, reconstruction and selection criteria, several asymmetries and ratios were estimated in order to study the W boson and the top quark polarizations. At 10 fb^{-1}, the results obtained were:

$$
\begin{aligned}
A_{FB} &= -0.194 \pm 0.024(sta) \pm 0.036(sys) \\
A_{+} &= 0.588 \pm 0.030(sta) \pm 0.049(sys) \\
A_{-} &= -0.839 \pm 0.012(sta) \pm 0.014(sys) \\
A_{b} &= -0.146 \pm 0.027(sta) \pm 0.035(sys) \\
A_{\nu} &= -0.191 \pm 0.025(sta) \pm 0.022(sys) \\
A_{l} &= 0.428 \pm 0.031(sta) \pm 0.032(sys) \\
r_{\nu l} &= -0.446 \pm 0.067(sta) \pm 0.060(sys) \\
r_{bl} &= -0.342 \pm 0.067(sta) \pm 0.082(sys)
\end{aligned}
$$

The measurement of angular asymmetries in the Wtb vertex represents a study of W polarization with single top events using the Fast Simulation of the ATLAS detector complementing those on $t\bar{t}$. The measurement of spin asymmetries and its ratios is the first result on the single top channel allowing to search for new physics both on the top quark production and decay.

The systematic error is in general larger than the statistical error for most observables. This is not the case for A_ν and $r_{\nu l}$, however, both the systematic and statistical uncertanties are similar. In summary, this work shows that the measurement of these observables is possible in single top even though the systematic errors are larger than the ones from the $t\bar{t}$. Both single top and $t\bar{t}$ results [26] may be combined in a near future.

From these measurements, the limits on the anomalous couplings in the top quark decay were determined with 68.3% CL using TopFit [4, 5]. The combination of different observables, mainly the spin asymmetries ratios, turns out to be very useful to improve the limits on the anomalous couplings. Furthermore, due to its different dependence on the anomalous couplings of the Wtb vertex in comparison to other observables, the r_{bl} is very useful to improve the limits. Therefore, this observable provides to the single top quark production an import role on the search for new physics.

An increase of statistics in the systematic uncertainties evaluation may allow to improve these results and, therefore, the limits on the anomalous couplings.

This study performed in the single top channel together with the results from $t\bar{t}$ provide the limits on the search for new physics beyond Standard Model in the Wtb vertex.

Bibliography

[1] F. Abe et al. Observation of top quark production in $\bar{p}p$ collisions. *Phys. Rev. Lett.*, 74:2626–2631, 1995.

[2] S. Abachi et al. Observation of the top quark. *Phys. Rev. Lett.*, 74:2632–2637, 1995.

[3] V. M. Abazov et al. Search for single top quark production in p anti-p collisions at s**(1/2) = 1.96-TeV. *Phys. Lett.*, B622:265–276, 2005.

[4] J. A. Aguilar-Saavedra, J. Carvalho, Nuno Filipe Castro, Filipe Veloso, and A. Onofre. Probing anomalous W t b couplings in top pair decays. *Eur. Phys. J.*, C50:519–533, 2007.

[5] J. A. Aguilar-Saavedra. Single top quark production at LHC with anomalous Wtb couplings. *Nucl. Phys.*, B804:160–192, 2008.

[6] C. Amsler et al. Review of particle physics. *Phys. Lett.*, B667:1, 2008.

[7] Francis Halzen and Alan D. Martin. *Quarks and Leptons: An Introductory Course in Modern Particle Physics*. Wiley, 1984.

[8] I. Borjanovic et al. Investigation of top mass measurements with the ATLAS detector at LHC. *Eur. Phys. J.*, C39S2:63–90, 2005.

[9] Roberto Bonciani, Stefano Catani, Michelangelo L. Mangano, and Paolo Nason. NLL resummation of the heavy-quark hadroproduction cross-section. *Nucl. Phys.*, B529:424–450, 1998.

[10] Zack Sullivan. Understanding single-top-quark production and jets at hadron colliders. *Phys. Rev.*, D70:114012, 2004.

[11] John Campbell and Francesco Tramontano. Next-to-leading order corrections to W t production and decay. *Nucl. Phys.*, B726:109–130, 2005.

[12] CDF Colaboration. A Limit on the Top Quark Width and Lifetime using the Template Method in the Lepton plus Jets Channel at CDF II. *CDF Note*, 8953, 2007.

[13] J. A. Aguilar-Saavedra. A minimal set of top anomalous couplings. 2008.

[14] Gregory Mahlon and Stephen J. Parke. Single top quark production at the LHC: Understanding spin. *Phys. Lett.*, B476:323–330, 2000.

[15] P. Lebrun. Superconductivity and cryogenics for the Large Hadron Collider. CERN-LHC-PROJECT-REPORT-441.

[16] G. Aad et al. The ATLAS Experiment at the CERN Large Hadron Collider. *JINST*, 3:S08003, 2008.

[17] A. Airapetian et al. ATLAS calorimeter performance. CERN-LHCC-96-40.

[18] ATLAS high-level trigger, data acquisition and controls: Technical design report. CERN-LHCC-2003-022.

[19] R. W. L. Jones. ATLAS computing and the GRID. *Nucl. Instrum. Meth.*, A502:372–375, 2003.

[20] S. R. Slabospitsky and L. Sonnenschein. TopReX generator (version 3.25): Short manual. *Comput. Phys. Commun.*, 148:87–102, 2002.

[21] Torbjorn Sjostrand, Stephen Mrenna, and Peter Skands. PYTHIA 6.4 physics and manual. *JHEP*, 05:026, 2006.

[22] J. Pumplin et al. New generation of parton distributions with uncertainties from global QCD analysis. *JHEP*, 07:012, 2002.

[23] ATLAS note. *ATLFAST 2.0 - A fast Simulation package for ATLAS*, ATL-PHYS-98-131 1998.

[24] Nuno Filipe da Silva Fernandes de Castro. Study of the Wtb vertex structure at the ATLAS experiment. CERN-THESIS-2008-083.

[25] Filipe Manuel Almeida Veloso. Study of ATLAS sensitivity to FCNC top quark decays.

[26] J. A. Aguilar-Saavedra, J. Carvalho, Nuno Filipe Castro, A. Onofre, and F. Veloso. ATLAS sensitivity to Wtb anomalous couplings in top quark decays. *Eur. Phys. J.*, C53:689–699, 2008.